LITHOS 432–433 (2022) 106891

Contents lists available at ScienceDirect

LITHOS

journal homepage: www.elsevier.com/locate/lithos

Synthesis Paper

Continental growth during migrating arc magmatism and terrane accretion at Sikhote-Alin (Russian Far East) and adjacent northeast Asia

Jeremy Tsung-Jui Wu [a,*], Jonny Wu [a], Igor Alexandrov [b], Thomas Lapen [a], Hao-Yang Lee [c], Vitaly Ivin [b]

[a] Department of Earth and Atmospheric Sciences, University of Houston, Houston, USA
[b] Far East Geological Institute, Vladivostok, Russia
[c] Institute of Earth Sciences, Academia Sinica, Taipei, Taiwan

ARTICLE INFO

Keywords:
Continental growth
Continental arc
Sikhote-Alin
Northeast Asia
Accretionary margin
Highly fractionated granite

ABSTRACT

Net additions to the continental landmasses, or continental growth, is a process that has irrevocably shaped our environment throughout the Earth history. Studies of ancient orogens suggest that continental growth can be facilitated by plate tectonics-driven arc magmatism and material accretion along convergent margins. However, such details are not well-understood due to the geological complexity of ancient orogens. Specifically, the role of the magmatic arc and its contributions to growing an accretionary margin remains unclear. This study explores an under-studied, long-lived magmatic arc along a 1500 km-wide swath of the NE Asian continental margin between 42° to 52°N (i.e., Sikhote-Alin and adjacent NE China, Sakhalin, and Hokkaido). We present new igneous rock zircon U-Pb ages ($n = 93$) and geochemistry ($n = 61$) from Sikhote-Alin that complement limited published data ($n > 60$). We synthesize these data to reveal four episodes of arc magmatism at Sikhote-Alin, including (1) 134 to 120 Ma S-type, (2) 110 to 100 Ma I-type, (3) 95 to 52 Ma highly-evolved I-type, and (4) <46 Ma I-type. We then combine our new results with published data ($n > 600$) and geology from adjacent NE Asia to analyze overall magmatic trends during a ~ 1500 km trenchward migration of arc magmatism driven by Jurassic to Cenozoic juvenile terrane accretion. The young, growing continental margin was modified by arc magmatism with chemical compositions determined by: (1) generation from a mantle wedge mixed with 1.3–1.4% sediment component from the downgoing slab; and, (2) silica-enrichment from crustal magmatic differentiation. Here, convergent margin continental growth that involved crustal accretion and trenchward migrating arc magmatism show magma compositions that evolve from initial mantle source mixing followed by crustal differentiation.

1. Introduction

Active margin continental growth mainly occurs in accretionary orogens, where juvenile oceanic material and mantle-derived arc magma are added (e.g., Cawood et al., 2009; Condie, 2007; Sengör and Natal'In, 1996). The concept has been widely applied to ancient accretionary orogens such as the Proterozoic-aged eastern Australian orogen (Glen, 2013; Kemp et al., 2009) and the Neoproterozoic to Mesozoic Central Asian orogenic belt (Fig. 1) (e.g., Kröner et al., 2014; Şengör et al., 2022; Xiao et al., 2020). One of the most recent examples of active margin continental growth is the West Pacific orogenic belt, a > 200 Ma ongoing growing margin along the eastern margin of Eurasia, the largest continent assembled through the Phanerozoic (Fig. 1). The West Pacific orogenic belt is an ideal place to study ongoing subduction/accretion processes during early-stage continental growth (Safonova et al., 2011; Şengör et al., 2022; Sengör and Natal'In, 1996; Zhu et al., 2021). New insights from this area may contribute to our understanding of magmatic arc evolution within laterally-growing accretionary orogens, which remains controversial (Gianni and Luján, 2021; Matsuda and Uyeda, 1971). A classic view of stepwise trench-ward magmatic arc migration correlated to continuous growth in accretionary orogen was initially described in Japan (Matsuda and Uyeda, 1971), but this has been challenged by the recognition of subduction erosion phases between episodic accretionary ages (Isozaki et al., 2010; Maruyama et al., 2011). Studies of western Pacific orogenic belt magmatism are also limited by later deformation from marginal sea opening during the Cenozoic, such

---

* Corresponding author.
E-mail addresses: twu20@uh.edu (J.T.-J. Wu), jwu40@central.uh.edu (J. Wu), tjlapen@central.uh.edu (T. Lapen), haoyanglee@earth.sinica.edu.tw (H.-Y. Lee).

https://doi.org/10.1016/j.lithos.2022.106891
Received 13 June 2022; Received in revised form 24 September 2022; Accepted 24 September 2022

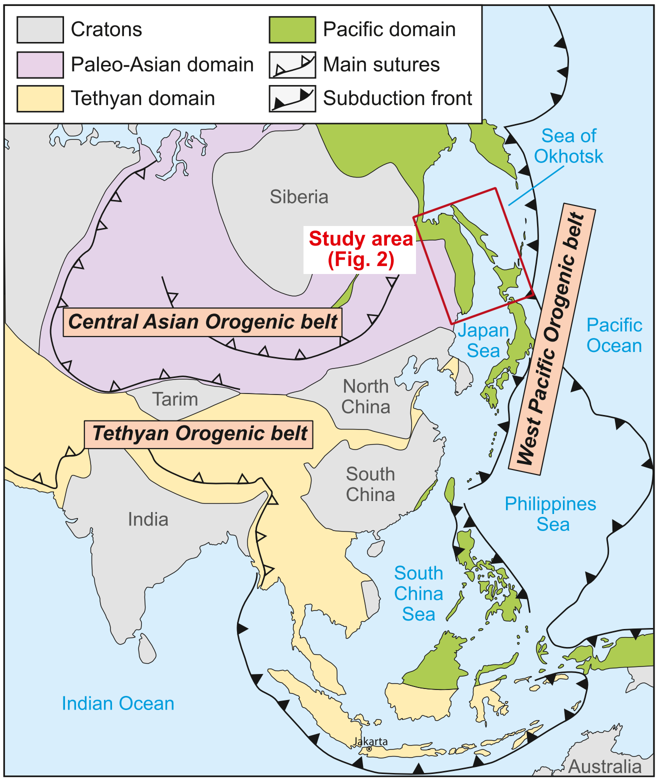

Fig. 1. Simplified tectonic map Asia (modified from Ren et al., 2013). The three Phanerozoic orogenic belts of Asia are shown: Central Asian, Tethyan, and the West Pacific orogenic belts. The study area is situated in the northern part of the West Pacific orogenic belt, where the Mesozoic to early Cenozoic geology was less deformed by Cenozoic marginal sea opening (e.g., Sea of Okhotsk, Japan Sea, Philippines Sea, and the South China Sea) relative to other areas of the margin.

as the Sea of Okhotsk, Japan Sea, Philippines Sea, and the South China Sea. (Fig. 1) (e.g., Baranov et al., 2002; Van Horne et al., 2017; Wu et al., 2016; Xu et al., 2014).

To give a closer examination of the magmatic arc behavior in a growing accretionary orogen, we focus on the ~1500 km-wide 42° to 52°N NE Asian margin at Sikhote-Alin (Russian Far East) and adjacent area (Figs. 1 and 2), which has been less deformed by the late Cenozoic marginal seas opening (Abrajevitch et al., 2012; Didenko et al., 2014; Khanchuk et al., 2015; Otofuji et al., 2002). We present new zircon U—Pb chronology ($n = 93$) and whole-rock geochemical data (61 major elemental, 52 trace elemental, and 22 Nd—Hf isotopic analysis) from igneous rocks across the Sikhote-Alin area. We combine our new igneous age and geochemical results with other published data ($n > 60$) from Sikhote-Alin that has been generally limited to the southern Sikhote-Alin (i.e., 42° to 47°N), and describe the igneous rock spatial-temporal distributions together with igneous rocks from adjacent NE Asia (i.e., Sakhalin in Russian Far East, Hokkaido, and NE China). We then discuss the spatiotemporal and geochemical evolution of the continental arc in northeast Asia between 160 Ma to the Present, and how arc magmatism responds to a laterally-growing continental margin.

2. Sampling and method

We collected 93 rock samples from Sikhote-Alin (Fig. 2 and Table 1), including 69 plutonic rocks, 15 volcanic rocks, and 9 pyroclastic rocks. Part of each rock sample was crushed and ground into powder for whole-rock geochemistry (i.e., major, trace element, Sm—Nd, and Lu—Hf isotopic analysis), and another part was used for zircon U—Pb chronology. For whole-rock geochemistry, we performed major and trace element analysis for 37 plutonic rocks and 15 volcanic rocks, and picked 22 rocks to proceed with Nd—Hf isotope geochemistry, while the 9 pyroclastic rocks only went through major element analysis.

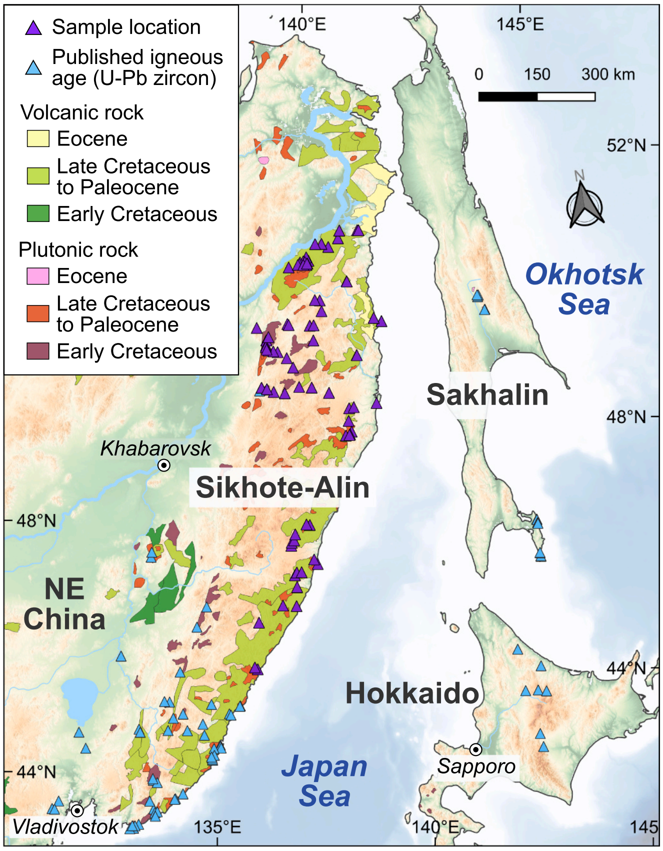

Fig. 2. Cretaceous to Cenozoic igneous rock distributions in NE Asia and sample locations of new analyses (purple triangles) and published ages (blue triangles). (For interpretation of the references to color in this figure legend, the reader is referred to the web version of this article.)

2.1. Zircon U—Pb dating

Zircon grains were separated from the 93 rock samples using conventional techniques and final purification by hand-picking. They were mounted in epoxy resin beds and half-sectioned after the resin bed had dried. For examination of zircon internal texture and selection of analytical spots, we took Cathodoluminescence (CL) and Energy Dispersive Spectrometer (EDS) images for the zircons, using an FEI XL30 Environmental Scanning Electron Microscope (ESEM) in the Jackson School of Geosciences at the University of Texas at Austin, and a JEOL JSM 6360LV SEM in the Institute of Earth Sciences at the Academia Sinica in Taiwan. We then conducted zircon U—Pb dating on three sets of Laser Ablation Inductively Coupled Plasma Mass Spectrometry (LA-ICP-MS) equipment: (1) an Analyte 193 coupled to a Varian 810 ICP-MS in the Department of Earth and Atmospheric Sciences at the University of Houston (see Shaulis et al., 2010 for details on the analytical procedure), which has the instrumental fractionation and drift calibrated by analyzing standard zircon Plešovice (337 ± 0.4 Ma) (Sláma et al., 2008), (2) an Analyte 193 coupled to an Agilent 7500 s ICP-MS in the Department of Geosciences at the National Taiwan University (see Chiu et al., 2013 for details on the analytical procedure), with the instrumental fractionation and drift calibration by analyzing standard zircon GJ-1 (601.7 ± 1.4 Ma) (Jackson et al., 2004), and (3) an Analyte 193 coupled to an Agilent 7900 s ICP-MS in the Institute of Earth Sciences at the Academia Sinica in Taiwan (See Quek et al., 2021 for details on the

Table 1
Result of zircon U—Pb dating for igneous rocks.

#	Sample	Rock name	Rock type	Lat (°N)	Lon (°E)	Age (Ma, 2σ error)			
1	KH16-01	granodiorite	plutonics	51.467	140.444	52.4	±	1.1	Mean age
2	KH16-03	granodiorite	plutonics	51.465	140.474	53.7	±	0.9	Mean age
3	KH16-04	granodiorite	plutonics	51.465	140.475	54.5	±	1.0	Mean age
4	KH16-08	granodiorite	plutonics	51.504	140.033	74.7	±	0.9	Mean age
5	KH16-09	basaltic andesite	volcanics	51.504	140.034	54.7	±	0.8	Intercept age
6	KH16-10	granodiorite	plutonics	51.504	140.035	76.8	±	0.6	Mean age
7	KH16-13	andesitic tuff	pyroclastics	51.396	139.975	75.0			Youngest peak
8	KH16-17	dacite	volcanics	51.294	139.720	63.4	±	1.0	Intercept age
9	KH16-20	granodiorite	plutonics	51.351	139.577	80.4	±	0.9	Intercept age
10	KH16-21	granodiorite	plutonics	51.354	139.575	80.4	±	1.0	Mean age
11	KH16-22	granodiorite	plutonics	51.365	139.429	84.0	±	1.2	Intercept age
12	KH16-24	basaltic andesite	volcanics	51.195	139.177	52.5	±	0.4	Mean age
13	KH16-27	quartz monzonite	plutonics	51.141	139.216	83.9	±	0.8	Mean age
14	KH16-28	quartz monzonite	plutonics	51.147	139.207	82.2	±	0.8	Mean age
15	KH16-29	granodiorite	plutonics	51.084	139.153	80.8	±	0.8	Mean age
16	KH16-31	granodiorite	plutonics	51.131	139.130	84.8	±	2.4	Intercept age
17	KH16-32	rhyolitic tuff	pyroclastics	51.106	138.960	87.0	±	0.9	Mean age
18	KH16-33	rhyolitic tuff	pyroclastics	51.119	138.994	83.7	±	0.6	Mean age
19	KH16-34	andesitic tuff	pyroclastics	51.136	139.017	85.2	±	0.9	Mean age
20	KH16-35	granodiorite	plutonics	51.092	139.084	83.8	±	0.5	Mean age
21	KH16-37	quartz monzonite	plutonics	51.112	139.103	84.7	±	0.7	Intercept age
22	KH16-39	andesitic tuff	pyroclastics	51.143	139.095	85.4	±	0.8	Mean age
23	KH16-40	granodiorite	plutonics	51.101	139.184	79.7	±	0.8	Intercept age
24	KH16-41	granodiorite	plutonics	51.103	139.173	82.9	±	0.8	Mean age
25	KH16-43	dacite	volcanics	51.089	138.739	84.6	±	1.1	Mean age
26	KH16-53	quartz monzodiorite	plutonics	50.285	137.787	52.1	±	0.4	Intercept age
27	KH16-55	granite	plutonics	50.002	137.934	72.3	±	2.1	Intercept age
28	KH16-56	granite	plutonics	49.981	137.924	110.5	±	0.9	Intercept age
29	KH16-60	granodiorite	plutonics	49.769	138.365	125.7	±	1.2	Mean age
30	KH16-64	granite	plutonics	49.615	138.478	109.4	±	1.9	Mean age
31	KH16-67	granite	plutonics	49.879	138.177	108.3	±	1.3	Mean age
32	KH16-68	quartz monzodiorite	plutonics	49.924	137.973	74.0	±	1.0	Mean age
33	KH16-69	granite	plutonics	49.943	137.935	73.0	±	0.4	Intercept age
34	KH16-71	granite	plutonics	50.123	138.022	70.5	±	0.9	Mean age
35	KH16-72	granodiorite	plutonics	50.077	137.966	123.9	±	0.9	Mean age
36	KH16-73	granite	plutonics	50.083	137.964	74.3	±	1.3	Intercept age
37	KH16-76	granite	plutonics	50.271	138.505	73.3	±	0.8	Mean age
38	KH16-77	granite	plutonics	50.252	138.529	71.6	±	0.8	Mean age
39	KH16-81a	basaltic andesite	volcanics	50.194	139.011	108.0			Youngest peak
40	KH16-81b	basaltic andesite	volcanics	50.194	139.011	75.6	±	0.9	Mean age
41	KH16-82	basalt	volcanics	50.190	139.101	72.1	±	1.2	Intercept age
42	KH16-84	monzodiorite	plutonics	50.161	140.505	62.0			Youngest peak
43	KH16-85	quartz monzodiorite	plutonics	50.160	140.505	75.6	±	0.6	Mean age
44	KH16-86	granodiorite	plutonics	50.158	140.506	63.0			Youngest peak
45	KH16-88	quartz monzodiorite	plutonics	50.093	140.672	66.2	±	0.9	Mean age
46	KH16-89	granodiorite	plutonics	50.096	140.672	87.4	±	0.9	Intercept age
47	KH16-92	granite	plutonics	50.759	140.018	78.5	±	2.0	Intercept age
48	KH16-93	granite	plutonics	50.754	140.020	53.9	±	0.6	Intercept age
49	KH16-97	tuff breccia	pyroclastics	50.540	139.331	63.1	±	0.5	Mean age
50	KH16-98	granite	plutonics	50.556	139.220	70.7	±	0.5	Mean age
51	KH16-99a	quartz monzodiorite	plutonics	50.380	139.333	81.7	±	0.5	Mean age
52	KH16-102a	granite	plutonics	49.968	139.040	71.6	±	1.3	Mean age
53	KH16-102b	granite	plutonics	49.968	139.040	122.3	±	2.0	Mean age
54	KH16-103a	diorite	plutonics	49.387	137.681	52.1	±	1.5	Intercept age
55	KH16-103b	granite	plutonics	49.389	137.680	109.3	±	1.7	Intercept age
56	KH16-103c	granite	plutonics	49.389	137.680	106.2	±	0.6	Intercept age
57	KH16-105a	granite	plutonics	49.354	137.797	107.8	±	0.9	Mean age
58	KH16-105b	granodiorite	plutonics	49.354	137.797	107.9	±	0.8	Mean age
59	KH16-107	granite	plutonics	49.297	137.943	57.6	±	1.2	Intercept age
60	KH16-110	granite	plutonics	49.251	138.193	106.6	±	1.0	Mean age
61	KH16-111	tuff	pyroclastics	49.312	138.545	53.5	±	0.5	Intercept age
62	KH16-114a	granite	plutonics	49.272	138.831	108.6	±	1.2	Mean age
63	KH16-114b	rhyolite	volcanics	49.272	138.831	58.6	±	0.5	Mean age
64	KH16-116a	granite	plutonics	49.152	139.209	84.0	±	0.7	Intercept age
65	KH16-116b	granite	plutonics	49.152	139.209	83.6	±	0.7	Mean age
66	KH16-118	diorite	plutonics	48.886	140.261	59.9	±	1.4	Intercept age
67	KH16-119	granodiorite	plutonics	48.514	139.588	59.6	±	1.1	Mean age
68	KH16-120	granite	plutonics	48.477	139.539	59.2	±	0.8	Mean age
69	KH16-122	granodiorite	plutonics	48.468	139.441	62.5	±	0.5	Mean age
70	KH16-123	granite	plutonics	48.467	139.526	59.9	±	0.6	Mean age
71	KH16-124	granodiorite	plutonics	48.683	139.557	60.1	±	1.1	Intercept age
72	KH16-126	granite	plutonics	48.872	139.614	66.8	±	0.9	Intercept age
73	KH16-127	granodiorite	plutonics	48.878	139.725	63.6	±	2.2	Intercept age
74	KH16-128	granite	plutonics	49.650	139.979	52.6	±	0.6	Mean age

(*continued on next page*)

Table 1 (*continued*)

#	Sample	Rock name	Rock type	Lat (°N)	Lon (°E)	Age (Ma, 2σ error)			
1	KH16-01	granodiorite	plutonics	51.467	140.444	52.4	±	1.1	Mean age
75	KH16-129	granodiorite	plutonics	49.648	139.984	82.4	±	1.9	Intercept age
76	P15-13	basalt	volcanics	46.426	137.765	65.0			Youngest peak
77	P15-20	quartz monzodiorite	plutonics	46.234	137.773	37.5	±	4.0	Intercept Age
78	P15-30	granodiorite	plutonics	45.016	136.571	67.9	±	0.7	Mean age
79	P16-01	rhyolitic tuff	pyroclastics	47.178	138.290	53.0	±	0.5	Mean age
80	P16-02	basaltic andesite	volcanics	47.194	138.214	62.0			Youngest peak
81	P16-04	granodiorite	plutonics	47.068	137.920	75.9	±	0.6	Mean age
82	P16-05	porphyritic rhyolite	volcanics	46.976	137.874	89.8	±	0.6	Mean age
83	P16-06	porphyritic andesite	volcanics	46.944	137.808	91.6	±	0.9	Mean age
84	P16-07	granodiorite	plutonics	46.900	137.789	90.8	±	1.0	Mean age
85	P16-08	granite	plutonics	46.627	138.263	58.8	±	0.6	Mean age
86	P16-09	granite	plutonics	46.546	138.328	58.4	±	0.7	Youngest peak
87	P16-16	granite	plutonics	46.457	137.930	63.6	±	0.6	Mean age
88	P16-17	porphyritic granite	plutonics	46.465	137.818	55.3	±	1.6	Mean age
89	P16-18	granodiorite	plutonics	46.229	137.773	43.0			Youngest peak
90	P16-19	porphyritic rhyolite	volcanics	45.932	137.691	66.3	±	0.5	Intercept Age
91	P16-22	rhyolitic tuff	pyroclastics	45.975	137.381	54.1	±	0.5	Intercept Age
92	P16-25	basalt	volcanics	45.763	136.770	65.0			Youngest peak
93	P16-28	rhyolite	volcanics	45.053	136.513	86.8	±	0.8	Mean age

analytical procedure), with calibration by analyzing standard zircon GJ-1 (601.7 ± 1.4 Ma) (Jackson et al., 2004). We performed data reduction through the software Iolite 2.5 (Paton et al., 2011), and calculated the age results using the Isoplot 4.15 (Ludwig, 2012). Standard zircons analyzed as unknown grains yielded the following $^{206}\text{Pb}/^{238}\text{Pb}$ weighted mean ages: 1053.0 ± 0.41 Ma (2σ, $n = 155$) from the zircon 91,500, 335.0 ± 0.3 Ma (2σ, $n = 104$) from the zircon Plešovice; 49.0 ± 0.2 Ma (2σ, $n = 46$) from the zircon T153.

2.2. Whole-rock major and trace element analyses

The powdered rock samples had proceeded with the loss on ignition (L.O·I) test and LiBO2 fusion digestion before the major element analysis. An Agilent 725 Inductively Coupled Plasma Optical Emission Spectrometer (ICP-OES) measured the major element composition of the sample solution in the Department of Earth and Atmospheric Sciences at the University of Houston (see Johnson et al., 2022 for details on the analytical procedure). The rock standard STM-1 was used for calibration of instrument sensitivity drift. The rock standards BHVO-2 and AGV-2 were analyzed repeatedly as unknown samples. They showed external reproducibility better than 4% (2σ) in all the elements.

The powdered rock samples had proceeded with microwave-assisted acid digestion before the trace element analysis. An Agilent 8800 ICP-QQQ-MS analyzed the trace element composition of the sample solution in the Department of Earth and Atmospheric Sciences at the University of Houston (See Johnson et al., 2022 for details on the analytical procedure). The rock standard BHVO-2 has been used for calibration of instrument sensitivity drift. The rock standards SCO-1, and AGV-2 were analyzed repeatedly as unknown samples. They showed external reproducibility of better than 5% (1σ) in most elements, except Li, Be, Sc, Zn, Rb, Y, and Sb, which yielded the reproducibility ranges from 5 to 10%.

2.3. Whole-rock Sm-Nd and Lu-Hf isotopic analyses

Before the isotope analysis, the powdered rock samples proceeded with microwave-assisted acid digestion and cation-exchange chromatography for Nd and Hf isolation. A NuPlasma II Multicollector-Inductively Coupled Plasma Mass Spectrometer (MC-ICP-MS) analyzed the Sm-Nd and Lu-Hf isotopic composition of the ~40 ppb Nd and ~ 40 ppb Hf sample solution, in the Department of Earth and Atmospheric Sciences at the University of Houston. The standard materials JNdi-1 ($^{143}\text{Nd}/^{144}\text{Nd} = 0.512115 \pm 0.000007$) (Tanaka et al., 2000) and JMC-475 ($^{176}\text{Hf}/^{177}\text{Hf} = 0.282163 \pm 0.000009$) (Blichert-Toft et al., 1997) were used for the calibrations on instrumental sensitivity drift. The standard materials BCR-2, JNdi-1, and JMC-475 were analyzed repeatedly as unknown samples. They show external reproducibility better than 0.003% (2σ) for $^{143}\text{Nd}/^{144}\text{Nd}$, and 0.006% (2σ) for $^{176}\text{Hf}/^{177}\text{Hf}$.

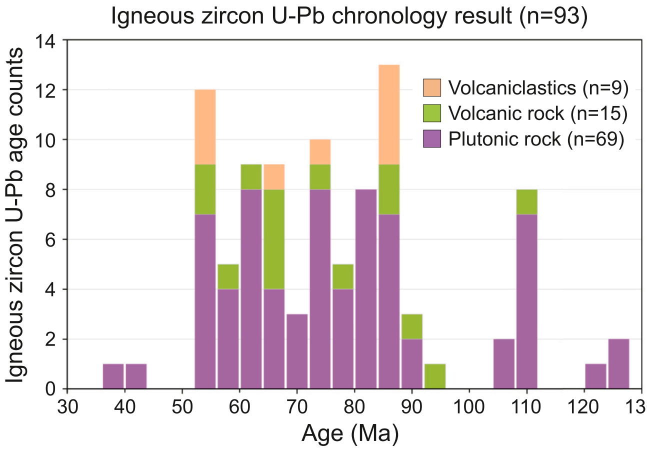

Fig. 3. Distribution of our new zircon U—Pb age results. Locations of the samples are shown in Fig. 1. See Table A. 1 for detailed results.

3. Result

3.1. Zircon U-Pb ages

We performed U-Pb chronology for >2000 zircon grains from the 93 rock samples in this study. A summary of the zircon U-Pb age results are given in Table 1 and Fig. 3, and detailed age data is in Table A. 1. The studied zircons generally show well-developed oscillatory zoning under CL images, with some grains also exhibiting sector zoning (Fig. A. 1). The zircon Th/U ratios range from 0.04 to 4, with a majority between 0.1 and 1.4 (Fig. 4). Igneous ages of the rocks were determined mainly by their weight-mean $^{206}\text{Pb}/^{238}\text{U}$ zircon age, or intercept age on Terra-Wasserburg and conventional Concordia Wetherill plots if the data shows the presence of common lead in some zircons (Tables 1 and A. 1). However, some samples have scattered zircon ages that may imply a presence of inherited grains, and a straightforward crystallization age is challenging to define. In this case, we use the youngest peak $^{206}\text{Pb}/^{238}\text{U}$ age as the determining igneous age. The igneous rock samples yield

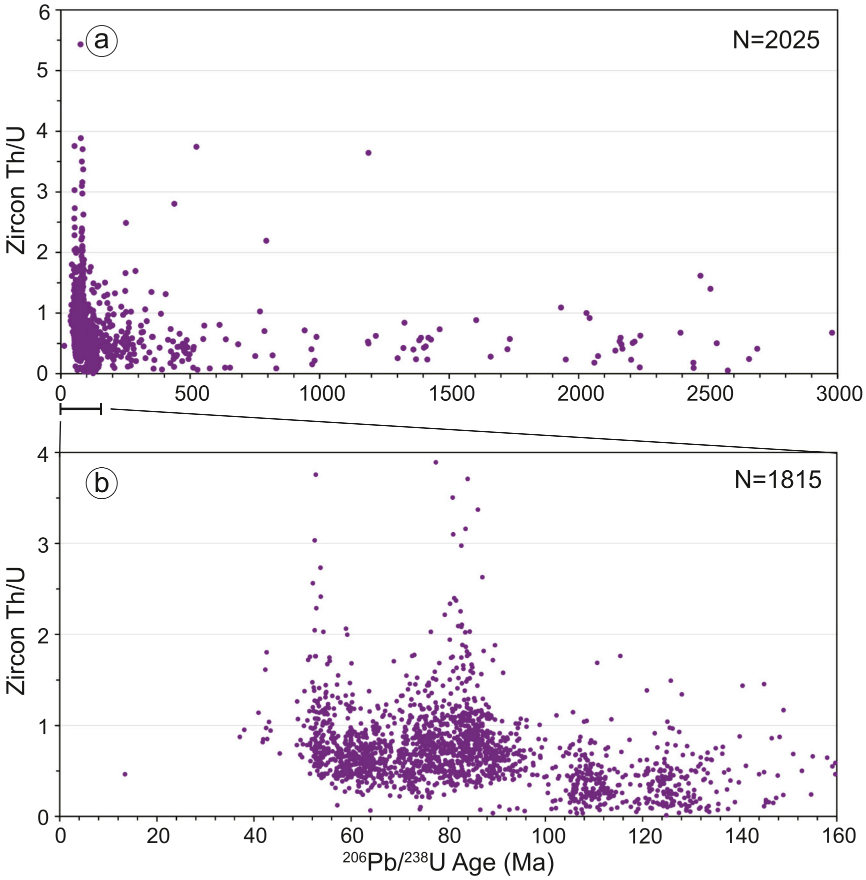

Fig. 4. Zircon Th/U ratio results. The zircons have single-grain $^{206}Pb/^{238}U$ ages that are mostly younger than 160 Ma ($n = 1815$), with limited occurrences of 3000 to 160 Ma ages ($n = 210$). They have Th/U ratios ranging between 0.01 and 5.4.

U—Pb zircon ages between 125.7 and 37.5 Ma (Table 1 and Fig. 3). Among the ~2000 analyzed zircons, there are ~230 inherited zircons with $^{206}Pb/^{238}U$ age older than 140 Ma, and ~ 70 of them yield Precambrian age (Fig. 4).

3.2. Whole-rock elemental composition

Whole-rock elemental analyses result were presented in Table A. 2 and Fig. A. 2. The 51 igneous rocks yield a wide range of volatile-free SiO_2 between 51 and 78% (Fig. 5b to 5c), including 39 acid rocks ($SiO_2 > 63\%$), 10 intermediate rocks ($SiO_2 = 52$ to 63%), and 3 basic rocks ($SiO_2 < 52\%$) (Le Maitre et al., 2005). The 9 pyroclastic rocks have a similar SiO_2 content range between 51 and 75%. The igneous rocks are identified as a calc-alkaline association in the cationic classification diagram (or the “Q-P" plot, Fig. 5a) (Debon and Le Fort, 1988), and calc-alkalic to calc-alkalic rocks in the modified alkali-lime index (Fig. 5c) (Frost and Frost, 2008). The plutonic rocks were plotted within the Metaluminous and Peraluminous fields in the A/CNK vs. A/NK diagram (Fig. 5d) (Maniar and Piccoli, 1989). Using the threshold A/CNK < 1.1 and CIPW normative corundum<1%, most of the plutonic rocks were defined as I-type granites, only 6 plutonic rocks are S-type granites with A/CNK > 1.1 and CIPW corundum >1% (Fig. 5d and Table A. 2) (Chappell and White, 2001). The Fe-index diagram (Frost and Frost, 2008) shows that most of the igneous rocks are the Magnesian type or Ferroan type with high silica content ($SiO2 > 70\%$), while two volcanic rocks are Ferroan type with intermediate silica content (Fig. 5e). The Y + Nb vs. Rb tectonic discrimination diagram (Pearce, 1996) reveals a volcanic arc origin for most of the igneous rocks (Fig. 5f). The Th-Hf-Ta plot (Wood, 1980) for mafic rocks agrees with this result (Fig. 5g). The C1 chondrite-normalized rare earth element (REE) diagram and primitive mantle-normalized multi-element spider diagram (Sun and McDonough, 1989) of the samples are shown in Fig. A. 2.

3.3. Whole-rock Nd-Hf isotopic composition

Whole-rock initial $^{143}Nd/^{144}Nd$ and $^{176}Hf/^{177}Hf$ ratios are calculated from the measured ratios using $^{147}Sm/^{144}Nd = (Sm/Nd)/1.645$, $^{176}Lu/^{177}Hf = (Lu/Hf)/1.992$ (Allègre, 2008), $\lambda^{147}Sm = 6.54 \times 10^{-12}$ y^{-1} (DePaolo and Wasserburg, 1976) and $\lambda^{176}Lu = 1.867 \times 10–11\ y^{-1}$ (Söderlund et al., 2004), and expressed as εNd(t) and εHf(t) values that compare the initial ratios of samples with those of a chondritic reservoir (CHUR) (Blichert-Toft and Albarède, 1997; Jacobsen and Wasserburg, 1980) at the igneous age time determined by U—Pb zircon chronology. The igneous rock samples yield a range of $\varepsilon Nd(t) = -6.6$ to $+5.5$ and $\varepsilon Hf(t) = -0.8$ to 12.8 (Fig. 6) that generally lie along a terrestrial Nd—Hf isotopic array (Vervoort et al., 1999).

4. Discussion

4.1. A summary of Sikhote-Alin igneous activity

4.1.1. Evolution of Early Cretaceous to Cenozoic Sikhote-Alin igneous activity

The Cretaceous to Cenozoic igneous rocks reveal magmatic activity along an understudied, long-lived ~1500 km wide continental margin along Sikhote-Alin area, Russian Far East (Fig. 2). Their significant implications for NW Panthalassa geodynamics and NE Asia continental crust evolution have been discussed in previous studies (e.g., Grebennikov et al., 2016; Jahn et al., 2015; Khanchuk et al., 2016; Khanchuk et al., 2019; Tang et al., 2016; Wu and Wu, 2019). However,

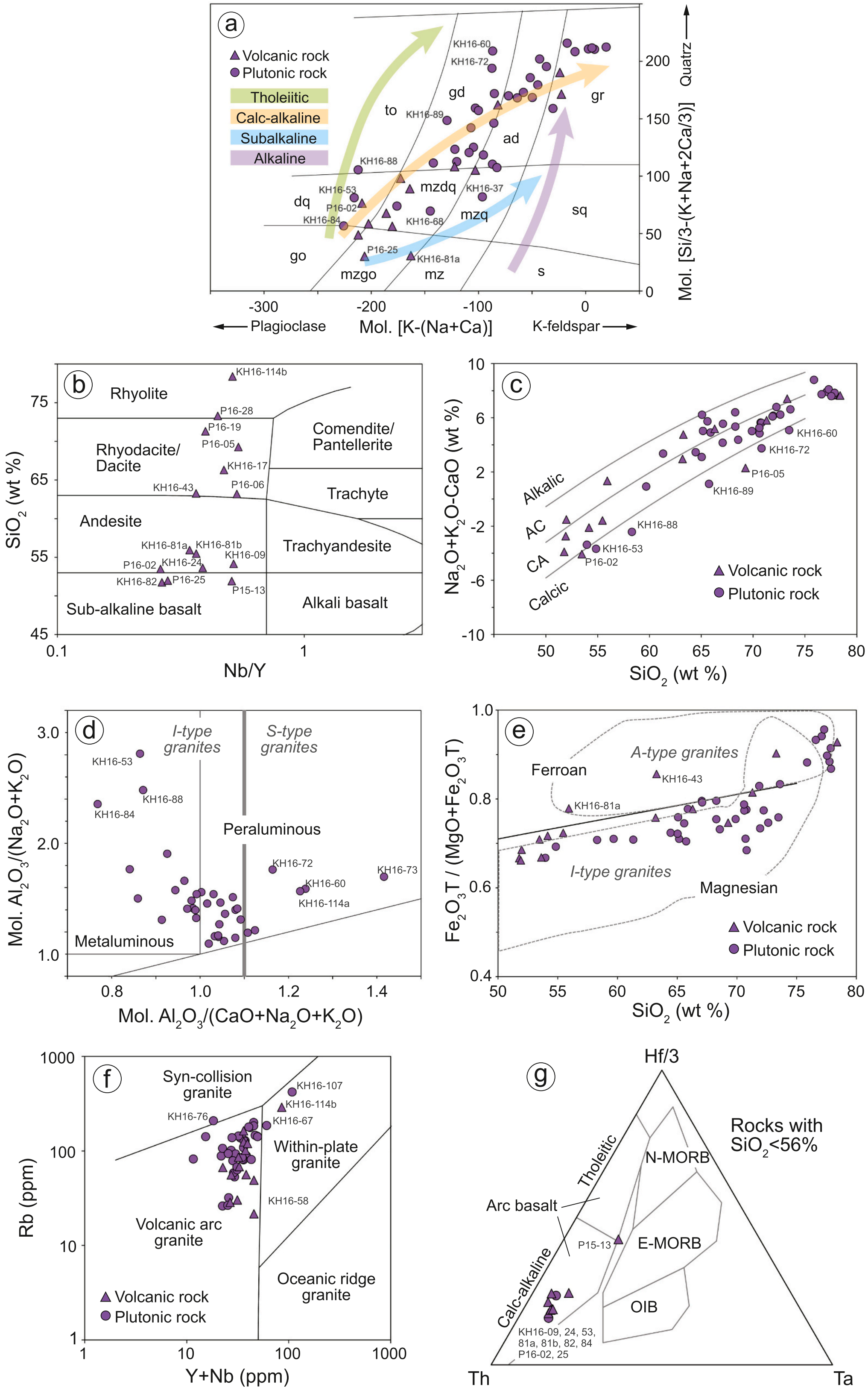

Fig. 5. Whole-rock geochemistry of the igneous rock samples. (a) the cationic classification diagram, or the “Q-P” plot (Debon and Le Fort, 1988). ad: adamellite (dellenite), dq: qtz diorite, qtz gabbro (qtz andesite, qtz basalt), gd: granodiorite, granogabbro (rhyodacite), go: gabbro, diorite (basalt, andesite), gr: granite (rhyolite), mz: monzonite (latite), mzdq: qtz monzodiorite, qtz monzo-gabbro (qtz lantiandesite, qtz latibasalt), mzgo: monzogabbro, monzodiorite (latibasalt, latiandesite), mzq: qtz monzonite (qtz latite), s: syenite (trachyte), sq.: qtz syenite (qtz trachyte), to: tonalite, trondjemite (dacite). (b) SiO_2 vs. Nb/Y diagram for volcanic rock (Winchester and Floyd, 1977). (c) the modified alkali-lime index diagram (Frost and Frost, 2008). AC: alkalic-calcic, CA: calc-alkalic. (d) the A/NK vs. A/CNK diagram for plutonic rock (Maniar and Piccoli, 1989) with an A/CNK = 1.1 boundary line between S- and I-type granites (Chappell and White, 1992). (e) the Fe-index diagram (Frost and Frost, 2008). (f) Rb vs. Y + Nb tectonic discrimination diagram (Pearce, 1996). (g) Th-Hf-Ta tectonic discrimination diagram for mafic rocks (Wood, 1980). N-MORB: normal mid-ocean ridge basalt, *E*-MORB: enriched mid-ocean ridge basalt, OIB: ocean island basalt. See Fig. A. 2 for normalized rare earth element and spidergram plots, and Table A. 2 for detailed whole-rock geochemistry results.

previous U—Pb zircon age and geochemical constraints for the igneous rocks have mainly come from the southern Sikhote-Alin margin (~500 km width) (light blue triangles in Fig. 2). The ~1000 km northern Sikhote-Alin margin is less explored and now newly constrained by our results (Fig. 2). To show a more complete Sikhote-Alin magmatic evolution history, we combine our new results for the northern Sikhote-Alin igneous rocks (*n* = 84, Table 1) with published data mainly from the southern Sikhote-Alin (*n* = 61) (Table A. 3) into a spatiotemporal zircon U—Pb age record (Figs. 7 and 8). For this compilation, we exclude our 9 samples of volcaniclastics because they may not be representative of in-

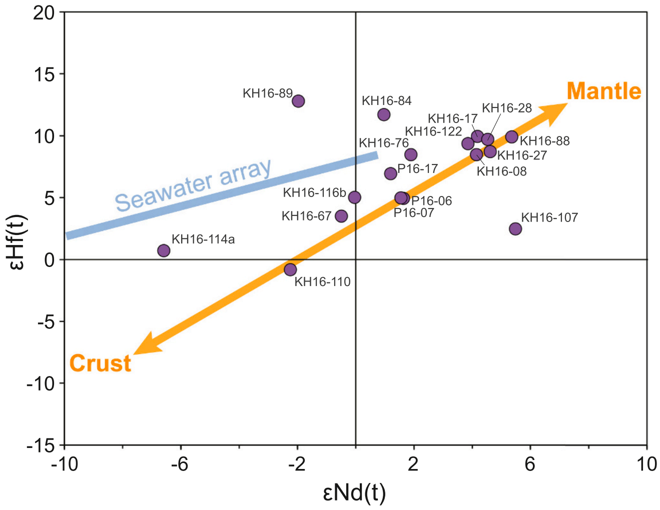

Fig. 6. Whole-rock Nd—Hf isotopic composition of rock samples in this study. Mantle-crust terrestrial array and seawater array after Vervoort et al. (1999). The studied igneous rocks generally have depleted Nd—Hf isotopic composition with εNd(t) = −6.6 to +5.5 and εHf(t) = −0.8 to 12.8. See Table A. 2 for detailed results.

situ magmatism. In addition, we synthesize an extensive whole-rock geochemistry database for 134 to 5 Ma Sikhote-Alin igneous rocks (Fig. 9) that includes our new data ($n = 52$) (Fig. 5) and published data ($n = 261$) (Table A. 4). Igneous ages are constrained by the 145 compiled zircon U—Pb ages in this study (Figs. 7 and 8), 32 whole-rock K—Ar ages, 2 biotite K—Ar ages, and a muscovite K—Ar age (References in Table A. 4).

The overall magmatic record shows four main episodes of Sikhote-Alin igneous activity (Fig. 8): (1) 134–120 Ma, (2) 110–100 Ma, (3) 95–52 Ma, and (4) <46 Ma, based on the >4 Myrs gaps in the U—Pb zircon igneous ages. The 134 to 52 Ma igneous rocks generally show subduction-related calc-alkalic characteristics (Fig. 9a) and magmatic arc signatures (Figs. 9b to d), i.e., enrichment in Th, Rb, and other large-ion lithophile element elements (LILE) relative to Ta, Hf, Y, Nb, and other high field strength elements (HFSE) (Pearce et al., 1984; Wood, 1980). In comparison, the younger 45 to 5 Ma Sikhote-Alin igneous rocks have a more complicated chemical composition that includes both continental arc and intra-plate signatures (Figs. 9b to d). All basalts with ages younger than 15 Ma have intraplate (Fig. 9b) and OIB or *E*-MORB signatures (Fig. 9d). Some published Sikhote-Alin igneous rocks with ages 132 to 98 Ma, and 46 to 39 Ma have adakitic signatures (Chashchin et al., 2011; Wu et al., 2017b), i.e., having whole-rock Sr/Y > 40 and La/Yb > 20 (Defant and Drummond, 1990; Moyen, 2009). However, the 125–105 Ma and 46–38 Ma samples in this study have moderate Sr/Y = 1 to 33, La/Yb = 7 to 19, and Eu depletion (Fig. A. 2) that is consistent with typical arc magmatism. These patterns reveal the complexity of Sikhote-Alin igneous genesis during the early Cretaceous and late Eocene, with both adakitic and typical arc rocks generated simultaneously.

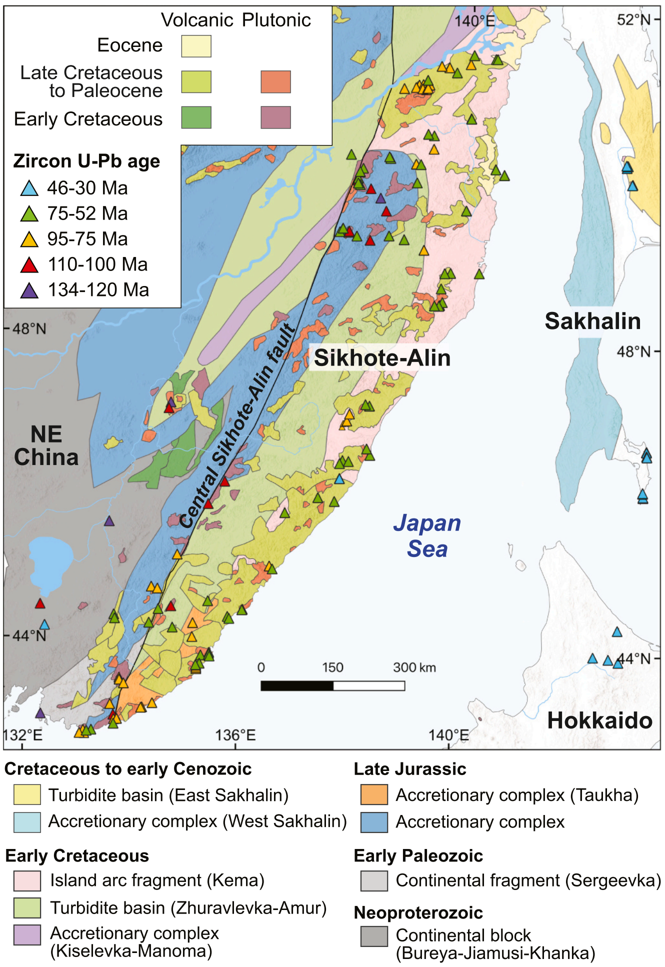

Fig. 7. Spatial distribution of igneous activity in Sikhote-Alin, Sakhalin, and Hokkaido constrained by U—Pb zircon chronology. The U—Pb zircon age database is our compilation of results from this study (n = 84) and other published data ($n = 95$) (Table A. 3). Igneous rocks with 134 to 100 Ma (purple and red triangles) were generally distributed in the Neoproterozoic and Jurassic geological units, those with 95 to 52 Ma ages (orange and green triangles) were mainly distributed in the Early Cretaceous units, and those with ages younger than 46 Ma have a more scattered distribution that mostly within Cretaceous to Cenozoic units. (For interpretation of the references to color in this figure legend, the reader is referred to the web version of this article.)

When using the S-I-A alphabet classification scheme (Chappell and White, 2001; Frost et al., 2001; Whalen et al., 1987) to classify the Sikhote-Alin plutonic rocks, nearly all the 134 to 120 Ma rocks were identified as S-type granites by their A/CNK >1.1 (Fig. 9e), average $Na_2O = 3.3\%$, restricted SiO_2 variation with 70.9 wt% average and $1\sigma = 2.1$ wt% ($n = 39$) (red circles in Fig. 9a). In comparison, most of the 110 to 52 Ma and 42 to 37 Ma plutonic rocks are I-type granites that have A/CNK <1.1 (Fig. 9e), higher average $Na_2O = 3.6\%$, CIPW corundum <1% (Table A. 2), and a broader spectrum of SiO_2 with 69.2 wt% in average and $1\sigma = 6.4$ wt% ($n = 221$) (Fig. 9a). Among the 110 to 52 Ma I-type granites (Fig. 9e), some 65 to 52 Ma felsic plutonic rocks also show high Fe/Mg, Ga/Al and slight enrichment in HFSE (e.g., Zr, Nb, Y and rare-earth elements like Ce). These may identify as A-type granites (Fig. 10a and b) (Grebennikov et al., 2016; Grebennikov and Maksimov, 2021; Grebennikov and Popov, 2014), and the "within-plate granite" in the Y + Nb vs. Rb plot (Fig. 9c). The A-type granites are significant because they are mostly associated with anorogenic/ post-orogenic/ extensional/ transform margin (strike-slip) environments (Grebennikov et al., 2016; Loiselle and Wones, 1979; Martin, 2006) (although not necessarily, according to Bonin, 2007; Whalen et al., 1987). However, it is not always straightforward to distinguish between A-type granite and highly fractionated I-type granite from their chemical signature (Bonin, 2007; Whalen et al., 1987; Wu et al., 2017a). We will further discuss the petrogenesis of the 65 to 52 Ma felsic rocks in Section 4.1.3.

Our synthesized datasets indicate episodic Cretaceous to Cenozoic arc magmatism (Figs. 8 and 9) in response to the Pacific-Panthalassa oceanic plate(s) subduction along the Sikhote-Alin margin, with magmatic hiatuses during early to middle Cretaceous (120 to 110 Ma, and 100 to 95 Ma), and early Eocene (52 to 46 Ma) (Fig. 8). The magmatic arc front along the NE Asian margin gradually moved away from Sikhote-Alin to the east (e.g., Sakhalin and Hokkaido) after 46 Ma, when intraplate magmatism occurred within Sikhote-Alin (Fig. 9b to d).

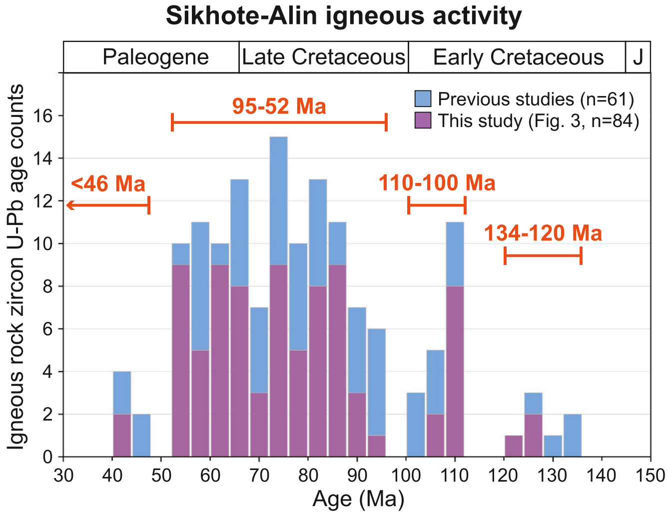

Fig. 8. Temporal distribution of Sikhote-Alin igneous activity constrained by U—Pb zircon chronology. The record shows four episodes of Sikhote-Alin igneous activity: (1) 134–120 Ma, (2) 110–100 Ma, (3) 95–52 Ma, and (4) <46 Ma, based on the >4 Ma gaps in <4 Myrs gaps in U—Pb zircon igneous ages. See Fig. 1 for the locations of published and our new samples.

The eastward arc migration could have been accelerated by the rapid 17.5 to 15.8 Ma Japan Sea opening (Hoshi et al., 2015). After 15 Ma, Sikhote-Alin magmatism has mainly intraplate signatures (Fig. 9b to d). The Cretaceous to Cenozoic Sikhote-Alin arc magmatism generally agrees with published NW Pacific plate reconstructions that show oceanic plate subduction along the Sikhote-Alin margin since at least the Mesozoic. Previous studies have proposed tectonic events in the middle Cretaceous and early Eocene periods that may correlate to the magmatic hiatus (Fig. 8), however, these events are debated. Some models suggest a transform NE Asian margin during early Cretaceous and early Cenozoic (Grebennikov et al., 2016; Grebennikov et al., 2021; Khanchuk et al., 2016; Khanchuk et al., 2019), early Cretaceous marginal sea closure (Arkhipov et al., 2019; Boschman et al., 2021; Ueda and Miyashita, 2005; Wu et al., 2022b), early Cenozoic spreading ridge subduction (Kimura et al., 2019; Liu et al., 2020; Nanayama et al., 2021; Seton et al., 2015; Wu et al., 2022a; Wu and Wu, 2019; Yamasaki et al., 2021) or marginal sea closure (Domeier et al., 2017; Ganbat et al., 2021).

4.1.2. *Late Cretaceous to early Eocene (95–52 Ma) highly evolved magmatism in Sikhote-Alin*

During the Late Cretaceous to early Cenozoic (95 to 52 Ma) the Sikhote-Alin magmatic arc shows a significantly higher average $SiO_2 =$ 70.0 wt% ($1\sigma = 6.7$, $n = 147$) when compared to the classic Cordilleran continental arcs that have average SiO_2 from 55.6 to 64.0 wt% in different areas (Ducea et al., 2015). In addition, the widely-distributed high silica magmatism along the ~1500 km Sikhote-Alin margin persisted for >40 Myrs, which is longer than those that have similar average SiO_2 in some areas of the Cordillera, which were limited in occurrence to a maximum of 20 Myrs (Kirsch et al., 2016). Here we discuss the petrogenesis of 95 to 52 Ma high silica magmatic rocks.

Silica saturation (i.e., high silica) in magmatic rocks can either result from the magmatic fractionation in the magma chamber or inherited from the source rock. Melting of a quartz-rich fertile sedimentary source rock is the original interpretation for an association of silica and aluminum saturation (i.e., A/CNK >1.1) in S-type granites (Chappell and White, 1992; Chappell and White, 2001), which is consistent with the 134 to 120 Ma S-type granites in Sikhote-Alin (average $SiO_2 = 70.9$ wt%, $1\sigma = 2.1$, $n = 39$) (Fig. 9e). However, most of the younger 110 to 52 Ma granites have I-type signatures that indicate aluminum undersaturation (i.e., A/CNK <1.1, Fig. 9e). Note that among all the 110 to 52 Ma I-type granites in Sikhote-Alin (Fig. 9e), the 95 to 52 Ma I-type granites have higher average silica contents (average $SiO_2 = 70.0$ wt%, $1\sigma = 6.7$, n = 147) compared to the 110 to 100 Ma I-type granites (average $SiO_2 = 67.6$ wt%, $1\sigma = 5.6$, $n = 74$).

On the other hand, high silica granites have been interpreted as the residual melt from an extensive crystallization differentiation during storage in crustal magma chambers (Bonin, 1999;Lee and Morton, 2015; Wu et al., 2017a). The extensive magmatic fractionation changes the chemistry of residual melt by increasing FeO*/MgO and incompatible elements (e.g., Li, K, Rb, and Cs), and decreasing Nb/Ta, Zr/Hf, compatible elements (e.g., Cr, Ni, and Co), and feldspar-compatible elements (Eu, Sr, and Ba) (Bau, 1996; Dostal and Chatterjee, 2000; Gelman et al., 2014; Lee and Morton, 2015; Wu et al., 2017a). When comparing to the geochemistry of older 134 to 100 Ma igneous rocks in Sikhote-Alin, most of the younger 95 to 52 Ma igneous rocks have higher FeO*/MgO (Fig. 10a), lower Zr/Hf, Nb/Ta, Ba, and stronger negative Eu anomaly (i.e., low Eu/Eu*) (Fig. 10c and d). These younger rocks fit a petrogenesis that involves extensive crystallization differentiation in their late-stage magmatic evolution. The decreasing Ba coincides with Eu/Eu* from part of the 95 to 52 Ma igneous rocks (Fig. 10d). This indicates the K-feldspar fractionation was the principal process during late-stage feldspar fractionation, since Ba is compatible in K-feldspar but incompatible in plagioclase, whereas Eu is compatible in the two feldspar types (Bachmann et al., 2005; Gelman et al., 2014).

In addition, extensive crystallization differentiation of silica-rich magma requires high temperature or enrichment volatiles to decrease the magma viscosity (Lesher and Spera, 2015). This prevents the elevated silica content and rising viscosity that causes the termination of further magma differentiation (Lee and Morton, 2015; Wu et al., 2017a). Although no estimated magma temperature (e.g., zircon saturation temperature) has been reported in Sikhote-Alin, the zircon Th/U might give some indications, since the high Th/U zircons imply their origin from a high-temperature magma without Th-bearing minerals (e.g., monazite or allanite) saturation (Harrison et al., 2007; Kirkland et al., 2015). Therefore, we newly compiled a Sikhote-Alin igneous zircon Th/U database (Fig. 11a) that includes numbers calculated from the new zircon U—Pb isotopic dating results ($n = 1788$, Fig. 4) and previous studies ($n = 729$) (Jahn et al., 2015; Zhao et al., 2017). The database reveals the 95 to 52 Ma zircons have a significantly higher average Th/U $= 0.96$ relative to an average Th/U $= 0.58$ from the 140 to 100 Ma zircons (Fig. 11b). Considering the high zircon Th/U corresponds to high zircon saturation temperatures (Harrison et al., 2007; Kirkland et al., 2015), this result could imply hotter 95 to 52 Ma magmatism compared to the 134 to 100 Ma magmatism in Sikhote-Alin. This would further support an interpretation that the 95 to 52 Ma Sikhote-Alin magmatism was highly fractionated under higher temperatures.

4.1.3. *A-type or highly fractionated I-type granites in Sikhote-Alin?*

The S-I-A alphabet classification for granites was designed to distinguish magma with different residual components (Chappell and White, 1992; Chappell and White, 2001; Whalen et al., 1987). However, classifying extremely felsic granites ($SiO_2 > 70\%$) can be difficult, for they have minimal residual components from extensive magmatic differentiation (Bonin, 2007; Chappell, 1999; White and Chappell, 1977). Particularly, HFSE enriched felsic granites can either be classified as highly fractionated I-type (Pérez-Soba and Villaseca, 2019; Qiu et al., 2017; Wu et al., 2003) or A-type granites (King et al., 2001). It is sometimes difficult to discriminate between the two granite types.

Previous studies suggest the 65 to 52 Ma felsic plutonic rocks in Sikhote-Alin are A-type granites associated with ignimbrites and volcanic rocks (Grebennikov et al., 2016; Grebennikov et al., 2021; Grebennikov and Maksimov, 2021; Grebennikov and Popov, 2014). According to our newly compiled database, Sikhote-Alin plutonic rocks with $10{,}000 \times Ga/Al > 2.6$ (i.e., one of the key definitions for A-type granite from Whalen et al., 1987) have a wider age range between 95 and 52 Ma (yellow and green triangles in Fig. 10b). However, the HFSEs (e.g., Zr, Nb, Ce, and Y) are not significantly enriched in these rocks

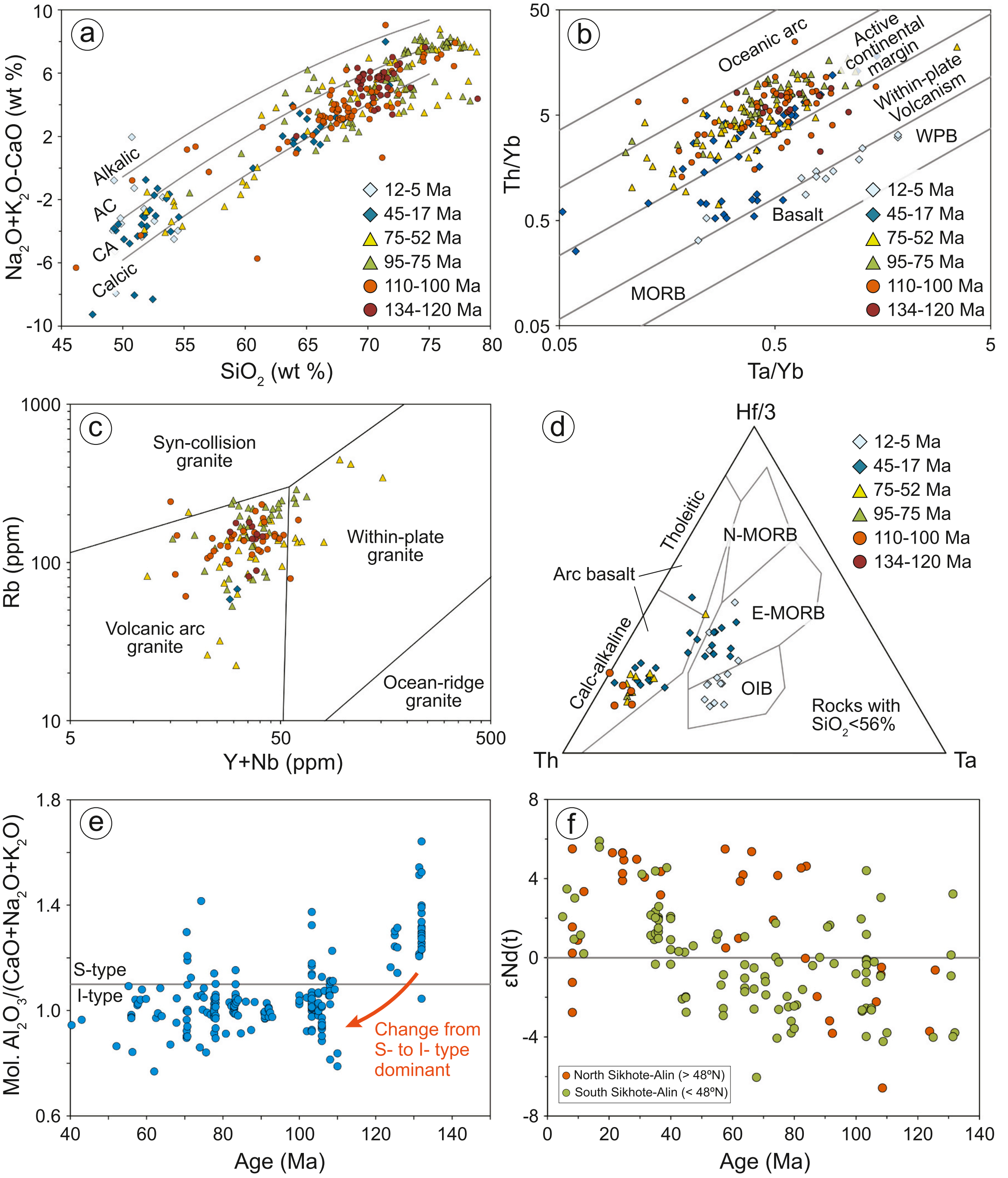

Fig. 9. Chemical-temporal evolution of Sikhote-Alin igneous activity. The whole-rock geochemistry dataset are synthesized from our new result ($n = 52$) (Table A. 2) and published data ($n = 261$) (Table A. 4). Samples are color-coded in Figs. 9a to 9d by igneous age groupings. (a) the modified alkali-lime index diagram (Frost and Frost, 2008), N-MORB: normal mid-ocean ridge basalt, E-MORB: enriched mid-ocean ridge basalt, OIB: ocean island basalt. (b) Ta/Yb vs. Th/Yb diagram (Gorton and Schandl, 2000), WPB: within-plate basalt, MORB: mid-ocean ridge basalt. (c) Y + Nb vs. Rb tectonic discrimination diagram for plutonic rock (Pearce et al., 1984), (d) Th-Hf-Ta tectonic discrimination diagram for mafic rocks (Wood, 1980). (e) Igneous age vs. A/CNK diagram with a S- and I-type granites discrimination following (Chappell and White, 1992). (f) Age vs. Nd isotopic composition plot of igneous rocks in northern and southern Sikhote-Alin. Samples are color-coded in Fig. 9f by their location either north or south of 48°N latitudes. The 134 to 52 Ma igneous rocks generally show calc-alkalic characteristics (Fig. 9a) and magmatic arc signature (Figs. 9b to d). In comparison, the younger 45 to 5 Ma Sikhote-Alin igneous rocks have a more complicated chemical composition that includes both continental arc and within plate signatures (Figs. 9b to d). All basalts with ages younger than 15 Ma have within-plate (Fig. 9b) and OIB or E-MORB signatures (Fig. 9d).

compared to typical S- and I- type granites (Fig. 10a and b). In addition, as previously discussed in sections 4.4.1 and 4.1.2, petrogenesis of some 95 to 52 Ma I-type granites (Fig. 9e) involved extensive crystallization differentiation (Fig. 10). Therefore, the high Ga/Al is likely a result of magmatic fractionation (Bonin, 1999; Whalen et al., 1987; Wu et al., 2017a) in the 95 to 52 Ma magmatism, rather than partial melting of a source rock that should generate significantly-enriched HFSEs A-type granite (Creaser et al., 1991; Eby, 1992; Martin, 2006). An alternative petrogenesis for the A-type granites in the region is fractionation from an alkalic and tholeiitic mafic magma (Bonin, 1999, 2007; Eby, 1992); however, alkalic and tholeiitic mafic rock is absent in our database for the 95 to 52 Ma magmatism in Sikhote-Alin. Instead, the 95 to 52 Ma

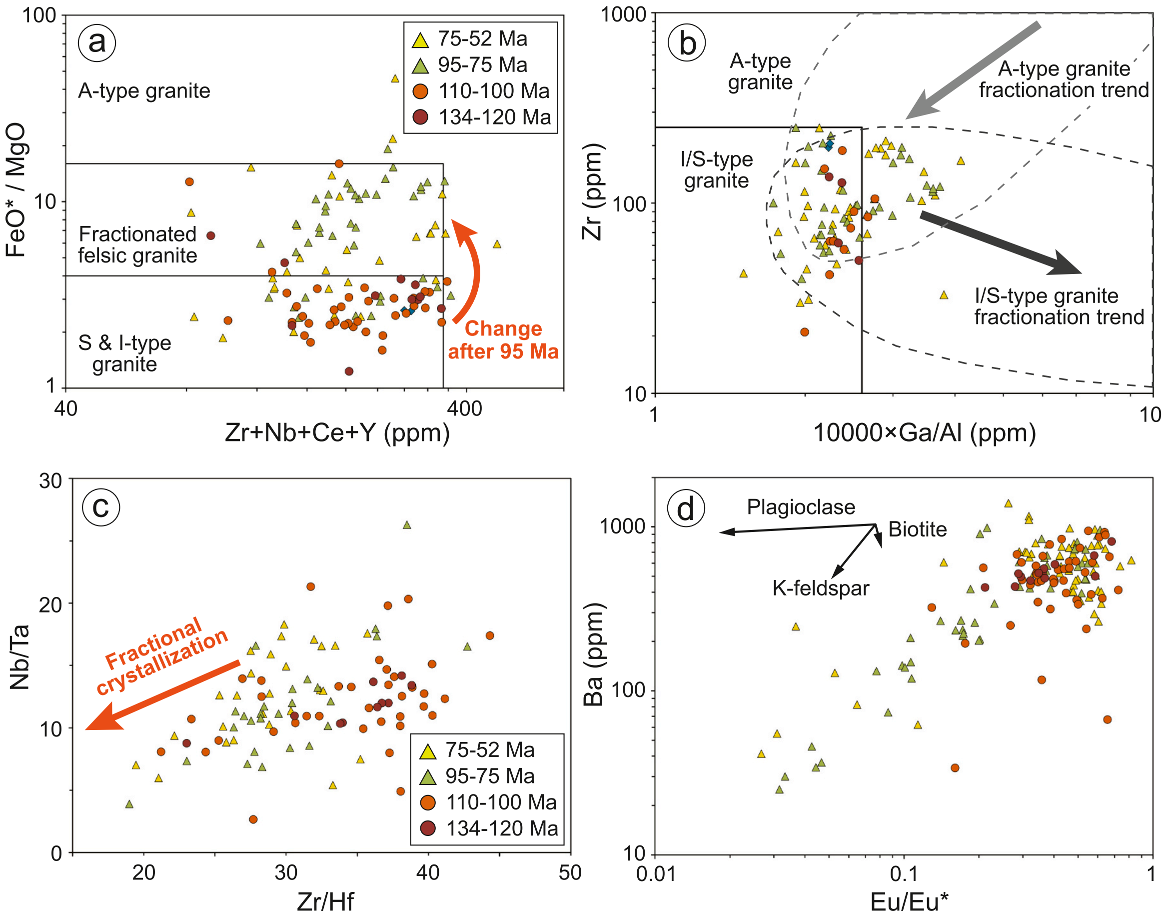

Fig. 10. Chemical indicators for magmatic fractionation. (a) Zr + Nb + Ce + Y vs. FeO*/MgO and (b) 10,000 × Ga/Al vs. Zr diagrams for plutonic rocks (Whalen et al., 1987) with the A-type and I/S-type granite fractionation trend (Wu et al., 2017a) (c) Zr/Hf vs. Nb/Ta and (d) Eu/Eu* vs. Ba plots as an indicator for magmatic differentiation (Bau, 1996; Dostal and Chatterjee, 2000; Wu et al., 2017a). Samples are color-coded by age groupings assigned in Fig. 9. When compared to the 134 to 100 Ma igneous rocks in Sikhote-Alin, most of the 95 to 52 Ma igneous rocks have higher FeO*/MgO, Ga/Al (Fig. 10a and b), lower Zr/Hf, Nb/Ta, Ba, and stronger negative Eu anomaly (i.e., low Eu/Eu*) (Fig. 10c and d), which fit a petrogenesis that involves extensive crystallization differentiation in their late-stage magmatic evolution.

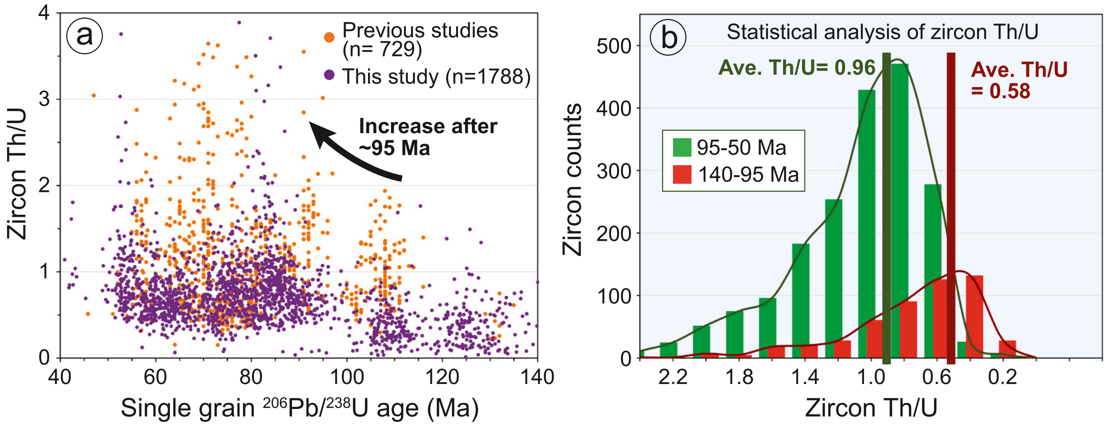

Fig. 11. Th/U of 140 to 40 Ma igneous zircons from Sikhote-Alin. (a) single-grain zircon $^{206}Pb/^{238}U$ age vs. zircon Th/U. (b) Statistical analysis of 140 to 95 Ma and 95 to 50 Ma igneous zircon Th/U. The 95 to 52 Ma zircons have a significantly higher average Th/U = 0.96 relative to an average Th/U = 0.58 from the 140 to 100 Ma zircons. Considering the high zircon Th/U corresponds to high zircon saturation temperatures (Harrison et al., 2007; Kirkland et al., 2015), this result could imply hotter 95 to 52 Ma magmatism compared to the 134 to 100 Ma magmatism in Sikhote-Alin.

mafic rocks with $SiO_2 < 56$ wt% show calc-alkaline compositions, revealed by their low to medium $Na_2O + K_2O\text{-}CaO = -4.1$ to -1.5 (Fig. 9a), low $Fe_2O_3T/(MgO + Fe_2O_3T) = 0.66$ to 0.72 ($n = 10$), and trace element composition enriched in LILE (e.g., Th) but depleted in HFSE (e.g., Hf and Ta) (Fig. 9d). Therefore, we conclude the Sikhote-Alin 95 to 52 Ma igneous rocks are mainly I-type granites. Some of them have gone through extensive fractionation that has caused their chemical composition to overlap with A-type granites (i.e., highly

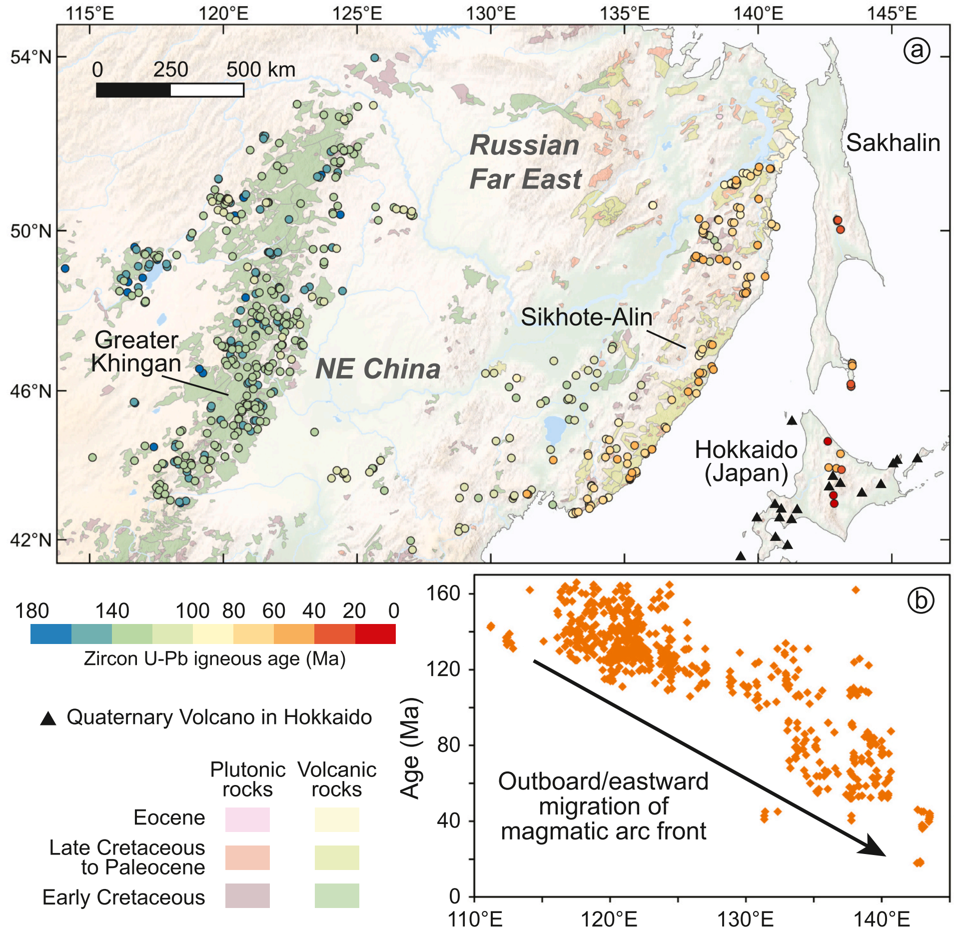

Fig. 12. 160 to 0 Ma outboard/eastward migration of 42°N to 54°N NE Asia magmatism. (a) Igneous rock distribution with U—Pb zircon age constraints in Sikhote-Alin, Sakhalin, Hokkaido (Table A. 3), and NE China (Gou et al., 2019 and references therein). (b) Present longitude vs. age of igneous rocks. The NE Asia igneous magmatic activity reveals a general eastward migration across a ~ 1700 km wide area from ~115°E to 143°E since 160 Ma. We exclude an average ~ 200 km eastward translation of the south Sakhalin and Hokkaido samples resulting from the Japan Sea opening, and consider a 160 Ma to present ~1500 km outboard/eastward migration of 42°N to 54°N NE Asia magmatism.

fractionated I-type granites).

4.2. *Implications for NE Asian margin continental growth*

4.2.1. *Magmatic arc migration along the growing NE Asia continental margin*

Continents mainly grow along active margins through the accretion of juvenile oceanic material and mantle-derived arc magmatism (Cawood et al., 2009; Condie, 2007; Sengör and Natal'In, 1996). Recycled crustal material may also be incorporated into the arc magmatic source region by dehydration and/or melting of the subducting slab, and may then re-enter the continental margin by arc magmatism (Stern, 2011). The NE Asian margin has been laterally growing through the Mesozoic to the Cenozoic, at least between the latitudes 42°N to 52°N, where juvenile terranes accreted since the Jurassic (Fig. 7) (Khanchuk et al., 2016). To further investigate the role of simultaneous arc magmatism-terrane accretion along the margin, we compiled a zircon U—Pb constrained ($n = 632$) spatiotemporal igneous history of NE Asia (Fig. 12), including Sikhote-Alin, Sakhalin, and Hokkaido (Table A. 3), and NE China (Gou et al., 2019) and references therein). The compiled database has low coverage in the area between Greater Khingan and Sikhote-Alin (Fig. 12a), where thick sediment covers the basement of the Songliao and Amur River basins. However, there are volcanic rocks with Jurassic to Early Cretaceous ages in the Songliao basin (Wang et al., 2006b).

The 160 Ma to present NE Asia igneous magmatic activity shows a general outboard/eastern migration across a ~ 1700 km wide area between 115°E and 143°E longitudes (Fig. 12b). Some Jurassic and early Cretaceous terranes (Samarka, Zhuravlevka-Amur, Kiselevka-Manoma, and West Sakhalin terranes) moved in a margin-parallel fashion (i.e., sinistral strike-slip) during early to middle Cretaceous on the order of hundreds to thousands of km (e.g., Abrajevitch et al., 2012; Didenko et al., 2014; Khanchuk et al., 2016; Liu et al., 2021; Peskov et al., 2019), but the margin-parallel movements generally ceased before the magmatism occurred in the terranes, and these movements do not materially affect our magma migration result (Fig. 7). In contrast, south Sakhalin and Hokkaido were displaced outboard by late Cenozoic Japan Sea opening <100 and < 300 km, respectively (Takeuchi et al., 1999), and these movements displaced the 46 to 18 Ma igneous rocks in the region. After excluding an average of ~200 km displacement in south Sakhalin and Hokkaido, our analyzed NE Asia magmatism between 42°N to 52°N still shows a ~ 1500 km eastward migration since 160 Ma.

NE Asia magmatism was not all linked to the westward subduction from the Pacific. A ~ 900 km eastward magmatic migration that occurred in 160 to 110 Ma NE China was a result of the rollback of the Panthalassa / Paleo-Pacific oceanic plate (Fig. 12) (Jing et al., 2021; Wang et al., 2006a; Wang et al., 2019; Wu et al., 2022b). An alternative idea links NE China magmatism to 160– 150 Ma *syn*-collision and 145–120 Ma post-collision tectonics, during and after the closure of the Mongol-Okhotsk Ocean (Wang et al., 2022; Zhang et al., 2018). The two tectonic events in the Pacific and Mongol-Okhotsk oceanic domains could dominate NE China geodynamics during the Jurassic to Early Cretaceous (Tang et al., 2022). Nevertheless, the 130–110 Ma Sikhote-Alin magmatic rocks were geochemically linked to subduction but post-collision setting (Fig. 9a to d). The magmatism since 130 Ma had stepwise migrated ~700 km eastward through the Jurassic to Cenozoic accreted juvenile terranes in Sikhote-Alin, Sakhalin, and Hokkaido (Figs. 7 and 12), and is likely an example for outboard / trenchward magmatic arc migration driven by laterally growing accretionary orogeny. Considering the NE Asian margin has Jurassic accretionary

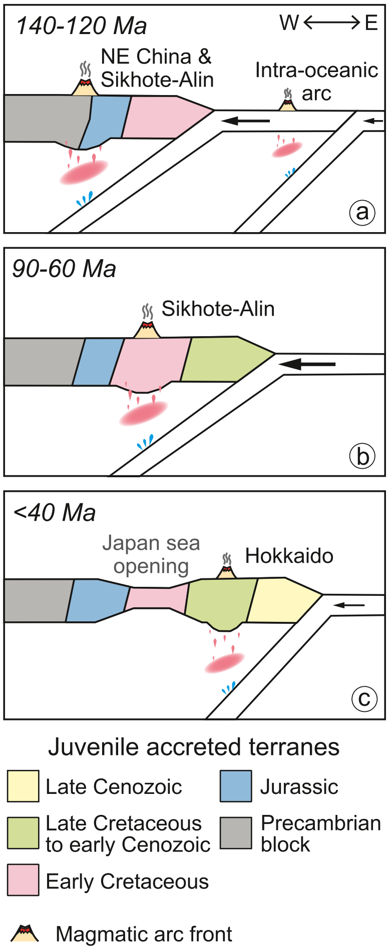

Fig. 13. Continental arc evolution of the 42°N to 52°N NE Asian margin from the Early Cretaceous to the present based on the result from this study. (a) Early Cretaceous (140 to 120 Ma): arc front moved from NE China into Jurassic accretionary belt in Sikhote-Alin (b) Late Cretaceous to early Cenozoic (90 to 60 Ma): arc front moved into early Cretaceous accreted terranes in Sikhote-Alin (c) Late Cenozoic (<25 Ma): the arc front moved entirely into the late Cretaceous to Cenozoic accretionary units in Hokkaido, after the Japan Sea opening.

complexes (Fig. 7) that are older than 130 Ma, magmatic migration links to the Pacific margin growth could be longer than ~700 km. Here we present a schematic model to summarize the continental growth and associated magmatic arc migration between 42°N to 52°N latitudes of the NE Asian margin since the Early Cretaceous (Fig. 13):

(1) Early Cretaceous (140 to 120 Ma) (Fig. 13a): the arc magmatism moved trenchward (Figs. 7 and 12) from inboard NE China into Sikhote-Alin. The early Cretaceous accretionary belt was developing along the margin. An intra-oceanic arc had accreted along the margin during 130–100 Ma (Arkhipov et al., 2019; Boschman et al., 2021; Ueda and Miyashita, 2005; Wu et al., 2022b). The early Cretaceous magmatism was emplaced within the Jurassic accretionary belt (Samarka, Nadanhada-Bikin, and Khabarovsk terranes) and Precambrian-early Paleozoic terranes (Bureya-Jiamusi-Khanka block and the Sergeevka terrane) (Fig. 7).

(2) Late Cretaceous to Paleocene (90 to 60 Ma) (Fig. 13b): the arc magmatism moved trenchward into the early Cretaceous terranes (Zhuravlevka-Amur and Kema) (Figs. 7 and 12). The late Cretaceous to Paleocene magmatism involved highly evolved magma characterized by their silica-enrichment (average $SiO_2 = 70.0$ wt %), Europium depletion, high Fe/Mg, and low Zr/Hf (Fig. 10).

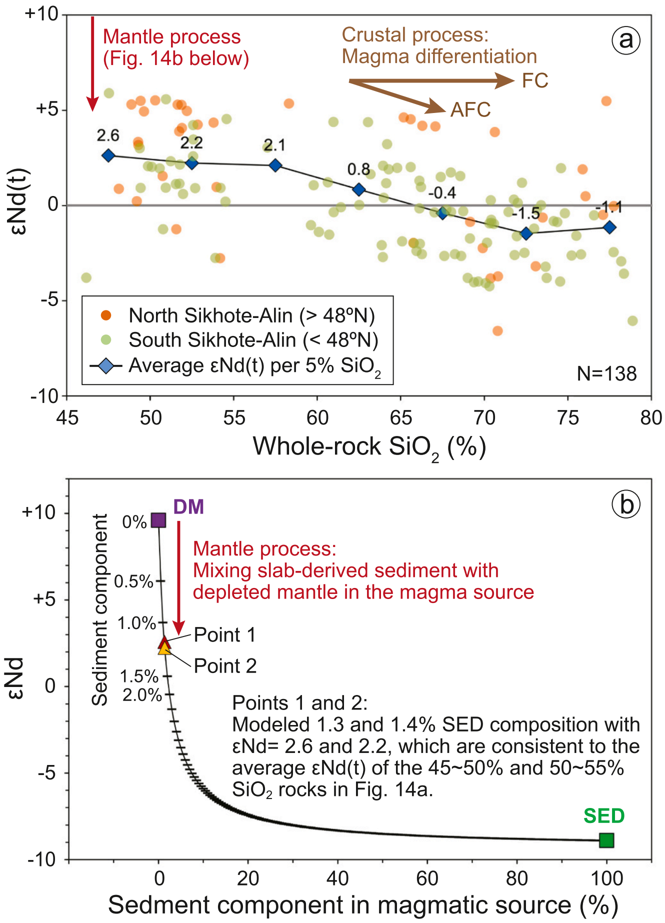

Fig. 14. Sikhote-Alin magma composition (whole-rock SiO_2 and εNd) determined by its mantle origin and evolution within the newly accreted continental crust. (a) The magmatism involved source mixing in the mantle (see Fig. 14b for details) that determined the Nd isotope composition of mafic rocks (45– 55% SiO_2 samples), and magma differentiation in the crust that resulted in significant SiO_2 enrichment and εNd(t) decreasing. The average εNd(t) of the samples calculated per 5% SiO_2 (blue diamonds) show that the mantle source mixing generates mafic rocks (SiO_2 = 45– 55%) with average εNd(t) between 2.2 and 2.6, and crustal assimilation had decreased the εNd(t) of more felsic rocks (SiO_2 = 55– 75%) from 2.2 to −1.5. AFC: assimilation-fractional crystallization, FC: fractional crystallization. (b) A two-end-member mixing model calculates the mixing between depleted mantle (DM) with Nd = 0.581 ppm and εNd = 9.6 (Workman and Hart, 2005), and sediment component (SED) from subducting slab, which has Nd = 27 ppm and εNd = −8.9 (Plank and Langmuir, 1998). The model shows that a mantle wedge includes 1.3– 1.4% sediment component has the εNd = 2.2– 2.6, which is consistent with the Nd isotopic composition of mafic rocks (SiO_2 = 45– 55%) in the Sikhote-Alin (Point 1 and 2). Point 1: average εNd = 2.6 from the 45– 50% SiO_2 Sikhote-Alin rocks in Fig. 14a. Point 2: average εNd = 2.2 from the 50– 55% SiO_2 Sikhote-Alin rocks in Fig. 14a. (For interpretation of the references to color in this figure legend, the reader is referred to the web version of this article.)

(3) Middle to late Cenozoic (<40 Ma) (Fig. 13c): the magmatic arc moved trenchward from Sikhote-Alin into the Late Cretaceous to early Cenozoic terranes in Sakhalin and Hokkaido area (Figs. 7 and 12). The arc front moved entirely away from Sikhote-Alin after the 20 to 15 Ma Japan Sea opening. Since then, <15 Ma basalts in Sikhote-Alin do not show arc signatures but instead show OIB and *E*-MORB characteristics (Fig. 9b and d).

4.2.2. *Chemical composition of arc magma controlled by crustal and mantle processes in NE Asia*

Arc magmatism along convergent margins generally initiates at a

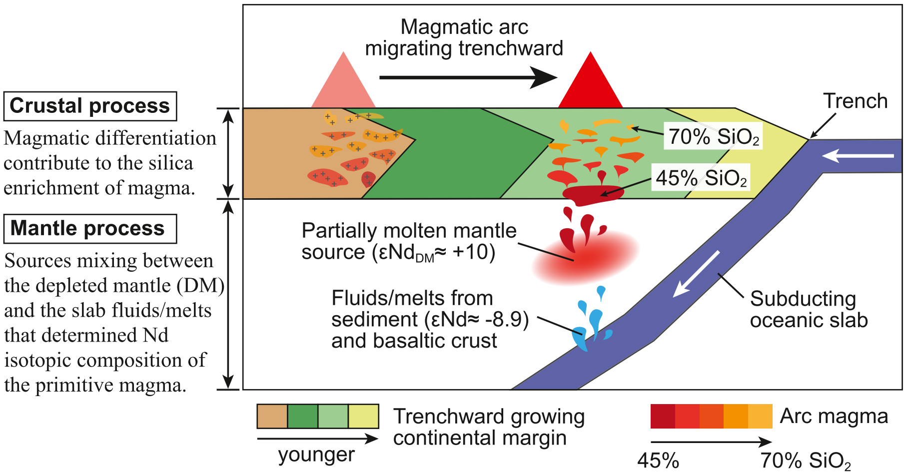

Fig. 15. Migrating magmatic arc in a growing continental margin with magma that generates and evolves from within-crust and mantle processes. The magmatic arc migrates trenchward corresponding to the retreating subducting oceanic slab in a growing continental margin. The lateral accreted material in the margin were color-coded by the accretion age with a trenchward younger trend. The magma in the continental crust was color-coded by their SiO_2 content from 45 to 75%. The chemical composition of the arc magma evolving through the mantle and within-crust process. The Nd isotope composition of the primitive/basaltic magma was determined mainly by source mixing between the mantle and subduction components (i.e., slab fluids and/or melts) in the partially molten mantle region. The within-crust magmatic differentiation (i.e., fractional crystallization and crustal assimilation) drive the silica enrichment of magma and increases its SiO_2 content. The input of evolving arc magma into the newly grown continental crust modified the new continent by adding mantle material and silica-enrichment with higher SiO_2 magma composition.

depth of around 100 km above the down-going slab (Syracuse and Abers, 2006). Magmatism occurs when the dehydrating subducted slab of oceanic lithosphere interacts with the mantle in the wedge of the overriding plate (Pearce and Peate, 1995; Schmidt and Jagoutz, 2017). Consequently, source mixing in the mantle wedge and magmatic differentiation within the overriding crust will determine arc magma chemical compositions. As discussed in section 5.1.2, Cretaceous to Cenozoic Sikhote-Alin magmatism involved magmatic evolution dominated by fractional crystallization (FC), resulting in significant SiO_2 enrichment (Figs. 9a, 10 and 14a). On the contrary, magma differentiation within the Sikhote-Alin crust had a smaller effect on the Nd isotopic magma composition, with average εNd(t) slightly decreasing by 3.6 from intermediate (average εNd(t) = 2.1 for 55– 60% SiO_2 samples) to silicic composition (average εNd(t) = −1.5 for 70– 75% SiO_2 samples) (Fig. 14a). This suggests that magmatic differentiation involving crustal contamination, such as assimilation-fractional crystallization (AFC) (DePaolo, 1981), has a limited effect on the isotopic composition of the continental arc magma. Alternatively, the Nd isotope composition of arc magma is mostly controlled by source mixing in the mantle wedge, which involves mantle source rock and subduction components (i.e., fluid and/or melt from subducting sediment). The mafic/primitive igneous rocks in Sikhote-Alin show a more enriched Nd isotopic composition (average εNd(t) = 2.6 for 45– 50% SiO_2 samples) (Fig. 14a) relative to a depleted mantle reservoir (i.e. εNd = +9.6) (Workman and Hart, 2005), which implies significant source mixing in the mantle wedge. When using a two-end-member mixing model between the depleted mantle (Nd = 0.581 ppm, εNd = +9.6) (Workman and Hart, 2005) and an average global subducting sediment (Nd = 27 ppm, εNd = −8.9) (Plank and Langmuir, 1998), we show that the average εNd(t) value of 45– 55% SiO_2 Sikhote-Alin igneous rocks is consistent with depleted mantle source mixed with 1.3– 1.4% sediment components (Fig. 14b).

4.2.3. *Implication for continental growth along the accretionary margin*

The Sikhote-Alin arc magma silica and radiogenic isotopic compositions are asymmetrically controlled by magmatic evolution in the crust and source mixing in the mantle (Fig. 14). Considering that magmatism both migrated through and also cooled within the growing accretionary margin lithosphere (Figs. 7 and 12), the magmatism should also have modified the overall composition of the juvenile accreted crust, with magma volume and its evolution determining the magnitude of crustal modification. Thus, the Sikhote-Alin and adjacent NE Asian margin is an example of significant crustal modification by widespread Cretaceous magmatism (Fig. 7) that involved 1.3– 1.4% sediment input in the arc magma generation region (i.e., mantle wedge) and silica-enrichment from significant magmatic differentiation in the arc crust (Fig. 14).

We summarize the magmatic evolution and crustal modification from magma input in a growing accretionary margin using a schematic model (Fig. 15):

1. Magmatic arc migrates trenchward in a lateral growing accretionary margin, associated with the trenchward migration of subducting oceanic slab and the magma source region in the mantle wedge.
2. The primitive basaltic arc magma generated from the mantle wedge has a chemical composition resulting from sources-mixing between the mantle melts, the subduction zone fluid and/or melts. The mixing ratio between the mantle and subduction components can be determined by the Nd isotopic composition of primitive basaltic rocks, or by other radiogenic isotopes with similar approaches, e.g., Hf, Pb and Sr.
3. The arc magma undergoes silica enrichment (i.e., increasing magma SiO_2%) through within-crust magmatic differentiation, which involves fractional crystallization (FC) and crustal assimilation. Although the latter mechanism may also control the Nd isotope composition, this was not significant in Sikhote-Alin magmatism (Fig. 14) even though some portions experienced significant magma differentiation (Figs. 10 and 14).
4. The arc magma brings mantle material into the newly-grown continental crust from the bottom-up and may drives the silica-enrichment of the juvenile crust with more felsic composition due to magmatic differentiation.

5. Conclusion

In this study, we present new zircon U—Pb age ($n = 93$) and whole-rock geochemical data ($n = 61$) from igneous rock across Sikhote-Alin (Russian Far East). We combined our new result with published data ($n > 60$) and showed four episodes of magmatism along a ~ 1500 km-wide NE Asian margin at Sikhote-Alin since the Early Cretaceous: (1) 134 to 120 Ma S-type magmatism, (2) 110 to 100 Ma I-type magmatism, (3) 95 to 52 Ma highly evolved I-type magmatism, and (4) <46 Ma I-type magmatism. The 134 to 52 Ma igneous rocks are generally calc-alkaline rocks with magmatic arc signature (i.e., enriched in LILE relative to HFSE), and εNd(t) isotopic values between −7 to +6. The 95 to 52 Ma episode has a significantly silica-enriched composition (average SiO_2 =

70.0 wt%) resulting from extensive crystallization differentiation.

We compiled a zircon U—Pb constrained spatiotemporal igneous history between 42°N to 52°N latitude of NE Asia (NE China, southern Russian Far East, and Hokkaido), and discussed it with regional geology. The result implies a growing NE Asian continental margin during the Mesozoic to the Present, with Jurassic to Cenozoic juvenile terrane accretion followed by a ~ 1500 km trench migration of arc magmatism since 160 Ma. The newly grown continental margin has been modified by the widespread arc magma, which was generated from the mantle wedge with 1.3– 1.4% sediment component, and had silica-enrichment from the magmatic differentiation in the crust.

Declaration of Competing Interest

The authors declare that they have no known competing financial interests or personal relationships that could have appeared to influence the work reported in this paper.

Acknowledgements

Jeremy Tsung-Jui Wu and Jonny Wu were supported by the National Science Foundation NSF CAREER grant EAR-1848327. J. T. J. Wu and J. Wu acknowledge support from the GURI Funds provided by the State of Texas and the University of Houston. Fieldwork studies at the Sikhote-Alin was supported by Russian Foundation for Basic Research (Research Project No. 15-55-52035). We sincerely thank Terri Tang, Minako Righter, Kuo-lung Wang, Yongjun Gao, Weihang Yang, Weiyao Yan, Yi-Peng Li, James Lavada Maner, Pan Zhao, Alan Wang, Yi-Ju Hsin, and Chien-Hui Hung for their generous supports on sample handling and lab works. We thank the two anonymous reviewers for their helpful comments on earlier draft of the manuscript. The late Bor-ming Jahn conducted the Russia-Taiwan research cooperation for years that was deeply appreciated and inspired this study.

Appendix A. Supplementary data

Supplementary data to this article can be found online at https://doi.org/10.1016/j.lithos.2022.106891.

References

Abrajevitch, A., Zyabrev, S., Didenko, A.N., Kodama, K., 2012. Palaeomagnetism of the West Sakhalin Basin: evidence for northward displacement during the cretaceous. Geophys. J. Int. 190 (3), 1439–1454.

Allègre, C.J., 2008. Isotope Geology. Cambridge University Press.

Arkhipov, M.V., Voinova, I.P., Kudymov, A.V., Peskov, A.Y., Otoh, S., Nagata, M., Golozubov, V.V., Didenko, A.N., 2019. Comparative analysis of Aptian–Albian rocks of the Kema and Kiselevka–Manoma Terranes. Geochem. Geochronol. Paleomagnet. Russian J. Pac. Geol. 13 (3), 239–264.

Bachmann, O., Dungan, M., Bussy, F., 2005. Insights into shallow magmatic processes in large silicic magma bodies: the trace element record in the Fish Canyon magma body, Colorado. Contrib. Mineral. Petrol. 149 (3), 338–349.

Baranov, B., Wong, H.K., Dozorova, K., Karp, B., Lüdmann, T., Karnaukh, V., 2002. Opening geometry of the Kurile Basin (Okhotsk Sea) as inferred from structural data. Island Arc 11 (3), 206–219.

Bau, M., 1996. Controls on the fractionation of isovalent trace elements in magmatic and aqueous systems: evidence from Y/Ho, Zr/Hf, and lanthanide tetrad effect. Contrib. Mineral. Petrol. 123 (3), 323–333.

Blichert-Toft, J., Albarède, F., 1997. The Lu-Hf isotope geochemistry of chondrites and the evolution of the mantle-crust system. Earth Planet. Sci. Lett. 148 (1–2), 243–258.

Blichert-Toft, J., Chauvel, C., Albarède, F., 1997. Separation of Hf and Lu for high-precision isotope analysis of rock samples by magnetic sector-multiple collector ICP-MS. Contrib. Mineral. Petrol. 127 (3), 248–260.

Bonin, B., 1999. Alkaline rocks and geodynamics. Turk. J. Earth Sci. 7 (3), 105–118.

Bonin, B., 2007. A-type granites and related rocks: evolution of a concept, problems and prospects. Lithos 97 (1–2), 1–29.

Boschman, L.M., van Hinsbergen, D.J., Spakman, W., 2021. Reconstructing Jurassic-cretaceous intra-oceanic subduction evolution in the Northwestern Panthalassa ocean using ocean plate stratigraphy from Hokkaido, Japan. Tectonics 40 (8) e2019TC005673.

Cawood, P.A., Kröner, A., Collins, W.J., Kusky, T.M., Mooney, W.D., Windley, B.F., 2009. Accretionary orogens through Earth history. Geol. Soc. Lond., Spec. Publ. 318 (1), 1–36.

Chappell, B., 1999. Aluminium saturation in I-and S-type granites and the characterization of fractionated haplogranites. Lithos 46 (3), 535–551.

Chappell, B.W., White, A., 1992. I-and S-type granites in the Lachlan Fold Belt. Earth Environ. Sci. Trans. Roy. Soc. Edinb. 83 (1–2), 1–26.

Chappell, B.W., White, A.J., 2001. Two contrasting granite types: 25 years later. Aust. J. Earth Sci. 48 (4), 489–499.

Chashchin, A., Nechaev, V., Nechaeva, E., Blokhin, M., 2011. Discovery of Eocene adakites in Primor'e. In: Proceedings Doklady Earth Sciences, Vol. 438. Springer, pp. 744–749.

Chiu, H.Y., Chung, S.L., Zarrinkoub, M.H., Mohammadi, S.S., Khatib, M.M., Iizuka, Y., 2013. Zircon U–Pb age constraints from Iran on the magmatic evolution related to Neotethyan subduction and Zagros orogeny. Lithos 162, 70–87.

Condie, K.C., 2007. Accretionary orogens in space and time. Memoirs-Geological Society of America 200, 145.

Creaser, R.A., Price, R.C., Wormald, R.J., 1991. A-type granites revisited: assessment of a residual-source model. Geology 19 (2), 163–166.

Debon, F., Le Fort, P., 1988. A cationic classification of common plutonic rocks and their magmatic associations: principles, method, applications. Bull. Mineral. 111 (5), 493–510.

Defant, M.J., Drummond, M.S., 1990. Derivation of some modern arc magmas by melting of young subducted lithosphere. Nature 347 (6294), 662–665.

DePaolo, D.J., 1981. Trace element and isotopic effects of combined wallrock assimilation and fractional crystallization. Earth Planet. Sci. Lett. 53 (2), 189–202.

DePaolo, D.J., Wasserburg, G., 1976. Nd isotopic variations and petrogenetic models. Geophys. Res. Lett. 3 (5), 249–252.

Didenko, A., Khanchuk, A., Tikhomirova, A., Voinova, I., 2014. Eastern segment of the Kiselevka-Manoma terrane (Northern Sikhote Alin): paleomagnetism and geodynamic implications: Russian Journal of. Pac. Geol. 8 (1), 18–37.

Domeier, M., Shephard, G.E., Jakob, J., Gaina, C., Doubrovine, P.V., Torsvik, T.H., 2017. Intraoceanic subduction spanned the Pacific in the late Cretaceous–Paleocene: Science. Advances 3 (11) p. eaao2303.

Dostal, J., Chatterjee, A., 2000. Contrasting behaviour of Nb/Ta and Zr/Hf ratios in a peraluminous granitic pluton (Nova Scotia, Canada). Chem. Geol. 163 (1–4), 207–218.

Ducea, M.N., Saleeby, J.B., Bergantz, G., 2015. The architecture, chemistry, and evolution of continental magmatic arcs. Annu. Rev. Earth Planet. Sci. 43, 299–331.

Eby, G.N., 1992. Chemical subdivision of the A-type granitoids: petrogenetic and tectonic implications. Geology 20 (7), 641–644.

Frost, B.R., Frost, C.D., 2008. A geochemical classification for feldspathic igneous rocks. J. Petrol. 49 (11), 1955–1969.

Frost, B.R., Barnes, C.G., Collins, W.J., Arculus, R.J., Ellis, D.J., Frost, C.D., 2001. A geochemical classification for granitic rocks. J. Petrol. 42 (11), 2033–2048.

Ganbat, A., Pastor-Galán, D., Hirano, N., Nakamura, N., Sumino, H., Yamaguchi, Y., and Tsujimori, T., 2021, Cretaceous to miocene NW Pacific plate kinematic constraints: paleomagnetism and Ar–Ar geochronology in the Mineoka Ophiolite Mélange (Japan): J. Geophys. Res. Solid Earth, v. 126, no. 5, p. e2020JB021492.

Gelman, S.E., Deering, C.D., Bachmann, O., Huber, C., Gutierrez, F.J., 2014. Identifying the crystal graveyards remaining after large silicic eruptions. Earth Planet. Sci. Lett. 403, 299–306.

Gianni, G.M., Luján, S.P., 2021. Geodynamic controls on magmatic arc migration and quiescence. Earth Sci. Rev. 218, 1–36, 103676.

Glen, R., 2013. Refining accretionary orogen models for the Tasmanides of eastern Australia. Aust. J. Earth Sci. 60 (3), 315–370.

Gorton, M.P., Schandl, E.S., 2000. From continents to island arcs: a geochemical index of tectonic setting for arc-related and within-plate felsic to intermediate volcanic rocks. Can. Mineral. 38 (5), 1065–1073.

Gou, J., Sun, D.Y., Qin, Z., 2019. Late Jurassic–Early Cretaceous tectonic evolution of the Great Xing'an Range: geochronological and geochemical evidence from granitoids and volcanic rocks in the Erguna Block, NE China. Int. Geol. Rev. 61 (15), 1842–1863.

Grebennikov, A., Maksimov, S., 2021. Causes of the occurrence of A-type volcanic rocks in active continental margins (Southern Sikhote-Alin, Russian Far East). Russ. Geol. Geophys. 62 (2), 207–222.

Grebennikov, A., Popov, V., 2014. Petrogeochemical aspects of the Late Cretaceous and Paleogene ignimbrite volcanism of East Sikhote-Alin. Russian J. Pac. Geol. 8 (1), 38–55.

Grebennikov, A.V., Khanchuk, A.I., Gonevchuk, V.G., Kovalenko, S.V., 2016. Cretaceous and Paleogene granitoid suites of the Sikhote-Alin area (Far East Russia): Geochemistry and tectonic implications. Lithos 261, 250–261.

Grebennikov, A.V., Kemkin, I.V., Khanchuk, A.I., 2021. Paleocene–early Eocene post-subduction magmatism in Sikhote-Alin (Far East Russia): new constraints for the tectonic history of the Izanagi-Pacific ridge and the East Asian continental margin. Geosci. Front. 12 (4), 101142.

Harrison, T.M., Watson, E.B., Aikman, A.B., 2007. Temperature spectra of zircon crystallization in plutonic rocks. Geology 35 (7), 635–638.

Hoshi, H., Kato, D., Ando, Y., Nakashima, K., 2015. Timing of clockwise rotation of Southwest Japan: constraints from new middle Miocene paleomagnetic results: Earth. Planets Space 67 (1), 92.

Isozaki, Y., Aoki, K., Nakama, T., Yanai, S., 2010. New insight into a subduction-related orogen: a reappraisal of the geotectonic framework and evolution of the Japanese Islands. Gondwana Res. 18 (1), 82–105.

Jackson, S.E., Pearson, N.J., Griffin, W.L., Belousova, E.A., 2004. The application of laser ablation-inductively coupled plasma-mass spectrometry to in situ U–Pb zircon geochronology. Chem. Geol. 211 (1), 47–69.

Jacobsen, S.B., Wasserburg, G., 1980. Sm-Nd isotopic evolution of chondrites. Earth Planet. Sci. Lett. 50 (1), 139–155.

Jahn, B.M., Valui, G., Kruk, N., Gonevchuk, V., Usuki, M., Wu, J.T., 2015. Emplacement ages, geochemical and Sr–Nd–Hf isotopic characterization of Mesozoic to early Cenozoic granitoids of the Sikhote-Alin Orogenic Belt, Russian Far East: Crustal growth and regional tectonic evolution. J. Asian Earth Sci. 111, 872–918.

Jing, J.H., Yang, H., Ge, W.C., Dong, Y., Ji, Z., Jing, Y., Bi, J.H., Zhou, H.Y., 2021. Early Cretaceous crust–mantle interaction linked to rollback of the Palaeo-Pacific flat-subducting slab: constraints from the intermediate–felsic volcanic rocks of the northern Great Xing'an Range, NE China. Geol. Mag. 1–22.

Johnson, C.M., Zheng, X.Y., Djokic, T., Van Kranendonk, M.J., Czaja, A.D., Roden, E.E., Beard, B.L., 2022. Early Archean biogeochemical iron cycling and nutrient availability: New insights from a 3.5 Ga land-sea transition. Earth Sci. Rev. 228, 103992.

Kemp, A., Hawkesworth, C., Collins, W., Gray, C., Blevin, P., 2009. Isotopic evidence for rapid continental growth in an extensional accretionary orogen: the Tasmanides, eastern Australia. Earth Planet. Sci. Lett. 284 (3–4), 455–466.

Khanchuk, A.I., Didenko, A.N., Tikhomirova, A.I., Voinova, I.P., 2015. Paleomagnetism and geochemistry of the Kiselevka block of the Kiselevka-Manoma terrane (northern Sikhote-Alin): Geodynamic signifi cance: special Paper of the Geological Society of. America v. 513, 483–507.

Khanchuk, A., Kemkin, I., Kruk, N., 2016. The Sikhote-Alin orogenic belt, Russian South East: Terranes and the formation of continental lithosphere based on geological and isotopic data. J. Asian Earth Sci. 120, 117–138.

Khanchuk, A., Grebennikov, A., Ivanov, V., 2019. Albian–Cenomanian Orogenic Belt and Igneous Province of Pacific Asia. Russian J. Pac. Geol. 13 (3), 187–219.

Kimura, G., Kitamura, Y., Yamaguchi, A., Kameda, J., Hashimoto, Y., Hamahashi, M., 2019. Origin of the early Cenozoic belt boundary thrust and Izanagi–Pacific ridge subduction in the western Pacific margin. Island Arc 28 (5), e12320.

King, P., Chappell, B., Allen, C.M., White, A., 2001. Are A-type granites the high-temperature felsic granites? Evidence from fractionated granites of the Wangrah Suite. Aust. J. Earth Sci. 48 (4), 501–514.

Kirkland, C., Smithies, R., Taylor, R., Evans, N., McDonald, B., 2015. Zircon Th/U ratios in magmatic environs. Lithos 212, 397–414.

Kirsch, M., Paterson, S.R., Wobbe, F., Ardila, A.M.M., Clausen, B.L., Alasino, P.H., 2016. Temporal histories of Cordilleran continental arcs: Testing models for magmatic episodicity. Am. Mineral. 101 (10), 2133–2154.

Kröner, A., Kovach, V., Belousova, E., Hegner, E., Armstrong, R., Dolgopolova, A., Seltmann, R., Alexeiev, D., Hoffmann, J., Wong, J., 2014. Reassessment of continental growth during the accretionary history of the Central Asian Orogenic Belt. Gondwana Res. 25 (1), 103–125.

Le Maitre, R.W., Streckeisen, A., Zanettin, B., Le Bas, M., Bonin, B., Bateman, P., 2005. Igneous Rocks: A Classification and Glossary of Terms: Recommendations of the International Union of Geological Sciences Subcommission on the Systematics of Igneous Rocks. Cambridge University Press.

Lee, C.T.A., Morton, D.M., 2015. High silica granites: Terminal porosity and crystal settling in shallow magma chambers. Earth Planet. Sci. Lett. 409, 23–31.

Lesher, C.E., Spera, F.J., 2015. Thermodynamic and transport properties of silicate melts and magma. In: The Encyclopedia of Volcanoes. Elsevier, pp. 113–141.

Liu, K., Zhang, J., Xiao, W., Wilde, S.A., Alexandrov, I., 2020. A review of magmatism and deformation history along the NE Asian margin from ca. 95 to 30 Ma: transition from the Izanagi to Pacific plate subduction in the early Cenozoic. Earth Sci. Rev. 209, 103317.

Liu, K., Xiao, W., Wilde, S.A., Zhang, J., Alexandrov, I., Kasatkin, S.A., Ge, M., 2021. Syn-subduction strike-slip faults shape an accretionary orogen and its provenance signatures: insights from Sikhote-Alin in NE Asia during the Late Jurassic to Early Cretaceous. Tectonics 40 (7) e2020TC006541.

Loiselle, M., Wones, D., 1979. Characteristics and origin of anorogenic granites. In: Proceedings Geological society of America abstracts with programs, Vol. 11, p. 468.

Ludwig, K., 2012. User's manual for Isoplot 3.75: A geochronological toolkit for Microsoft Excel, 75 pp. Berkeley Geochronology Center, Special Publication, no. 5.

Maniar, P.D., Piccoli, P.M., 1989. Tectonic discrimination of granitoids. Geol. Soc. Am. Bull. 101 (5), 635–643.

Martin, R.F., 2006. A-type granites of crustal origin ultimately result from open-system fenitization-type reactions in an extensional environment. Lithos 91 (1–4), 125–136.

Maruyama, S., Omori, S., Senshu, H., Kawai, K., Windley, B., 2011. Pacific-type orogens: new concepts and variations in space and time from present to past. J. Geography (Chigaku Zasshi) 120 (1), 115–223.

Matsuda, T., Uyeda, S., 1971. On the Pacific-type orogeny and its model—extension of the paired belts concept and possible origin of marginal seas. Tectonophysics 11 (1), 5–27.

Moyen, J.F., 2009. High Sr/Y and La/Yb ratios: the meaning of the "adakitic signature". Lithos 112 (3), 556–574.

Nanayama, F., Tajika, J., Yamasaki, T., Kurita, H., Iwano, H., Danhara, T., Hirata, T., 2021. The emplacement of in situ greenstones in the northern Hidaka belt: the tectonic relationship between subduction of the Izanagi–Pacific ridge and Hidaka magmatic activity. Island Arc 30 (1), e12403.

Otofuji, Y.I., Matsuda, T., Enami, R., Uno, K., Nishihama, K., Su, L., Kulinich, R.G., Zimin, P.S., Matunin, A.P., Sakhno, V.G., 2002. Internal deformation of Sikhote Alin volcanic belt, far eastern Russia: paleocene paleomagnetic results. Tectonophysics 350 (3), 181–192.

Paton, C., Hellstrom, J., Paul, B., Woodhead, J., Hergt, J., 2011. Iolite: freeware for the visualisation and processing of mass spectrometric data. J. Anal. At. Spectrom. 26 (12), 2508–2518.

Pearce, J., 1996. Sources and settings of granitic rocks. Episodes 19, 120–125.

Pearce, J.A., Peate, D.W., 1995. Tectonic implications of the composition of volcanic arc magmas. Annu. Rev. Earth Planet. Sci. 23, 251–286.

Pearce, J.A., Harris, N.B., Tindle, A.G., 1984. Trace element discrimination diagrams for the tectonic interpretation of granitic rocks. J. Petrol. 25 (4), 956–983.

Pérez-Soba, C., Villaseca, C., 2019. Li-Na-metasomatism related to I-type granite magmatism: a case study of the highly fractionated La Pedriza pluton (Iberian Variscan belt). Lithos 344, 159–174.

Peskov, A.Y., Didenko, A., Kudymov, A., Karetnikov, A., Arkhipov, M., 2019. Paleomagnetism and petrochemistry of sandstones from the Gorinskaya and Pionerskaya Formations, Zhuravlevka–Amurian Terrane (Northern Sikhote Alin). Russian J. Pac. Geol. 13 (6), 556–567.

Plank, T., and Langmuir, C. H., 1998, The chemical composition of subducting sediment and its consequences for the crust and mantle: Chem. Geol., v. 145, no. 3–4, p. 325–394.

Qiu, Z., Yan, Q., Li, S., Wang, H., Tong, L., Zhang, R., Wei, X., Li, P., Wang, L., Bu, A., 2017. Highly fractionated early cretaceous I-type granites and related Sn polymetallic mineralization in the Jinkeng deposit, eastern Guangdong, SE China: Constraints from geochronology, geochemistry, and Hf isotopes. Ore Geol. Rev. 88, 718–738.

Quek, L.X., Lee, T.Y., Ghani, A.A., Lai, Y.M., Roselee, M.H., Lee, H.Y., Iizuka, Y., Lin, Y.L., Yeh, M.W., Amran, M.A., 2021. Tracing detrital signature from Indochina in Peninsular Malaysia fluvial sediment: possible detrital zircon recycling into West Borneo Cenozoic sediments. J. Asian Earth Sci. 218, 104876.

Ren, J.S., Niu, B.G., Wang, J., He, Z.J., Jin, X.C., Xie, L.Z., Zhao, L., Liu, R.Y., Jiang, X.J., Li, S., 2013. 1: 5 million international geological map of Asia. Diqiu Xuebao(Acta Geoscientica Sinica) 34 (1), 24–30.

Safonova, I., Seltmann, R., Kroner, A., Gladkochub, D., Schulmann, K., Xiao, W., Kim, J., Komiya, T., Sun, M., 2011. A new concept of continental construction in the Central Asian Orogenic Belt. Episodes 34 (3), 186–196.

Schmidt, M.W., Jagoutz, O., 2017. The global systematics of primitive arc melts. Geochem. Geophys. Geosyst. 18 (8), 2817–2854.

Sengör, A.C., Natal'In, B.A., 1996. Turkic-type orogeny and its role in the making of the continental crust. Annu. Rev. Earth Planet. Sci. 24 (1), 263–337.

Şengör, A.C., Sunal, G., Natal'in, B.A., van der Voo, R., 2022. The Altaids: a review of twenty-five years of knowledge accumulation. Earth Sci. Rev. 228, 104013.

Seton, M., Flament, N., Whittaker, J., Müller, R.D., Gurnis, M., Bower, D.J., 2015. Ridge subduction sparked reorganization of the Pacific plate-mantle system 60–50 million years ago. Geophys. Res. Lett. 42 (6), 1732–1740.

Shaulis, B., Lapen, T.J., Toms, A., 2010. Signal linearity of an extended range pulse counting detector: applications to accurate and precise U-Pb dating of zircon by laser ablation quadrupole ICP-MS. Geochem. Geophys. Geosyst. 11 (11).

Sláma, J., Košler, J., Condon, D.J., Crowley, J.L., Gerdes, A., Hanchar, J.M., Horstwood, M.S., Morris, G.A., Nasdala, L., Norberg, N., 2008. Plešovice zircon—a new natural reference material for U–Pb and Hf isotopic microanalysis. Chem. Geol. 249 (1), 1–35.

Söderlund, U., Patchett, P. J., Vervoort, J. D., and Isachsen, C. E., 2004, The 176Lu decay constant determined by Lu–Hf and U–Pb isotope systematics of Precambrian mafic intrusions: Earth Planet. Sci. Lett., v. 219, no. 3–4, p. 311–324.

Stern, C.R., 2011. Subduction erosion: rates, mechanisms, and its role in arc magmatism and the evolution of the continental crust and mantle. Gondwana Res. 20 (2–3), 284–308.

Sun, S.S., McDonough, W.F., 1989. Chemical and isotopic systematics of oceanic basalts: implications for mantle composition and processes. Geol. Soc. Lond., Spec. Publ. 42 (1), 313–345.

Syracuse, E.M., Abers, G.A., 2006. Global compilation of variations in slab depth beneath arc volcanoes and implications. Geochem. Geophys. Geosyst. 7, no. 5.

Takeuchi, T., Kodama, K., Ozawa, T., 1999. Paleomagnetic evidence for block rotations in Central Hokkaido–south Sakhalin, Northeast Asia. Earth Planet. Sci. Lett. 169 (1–2), 7–21.

Tanaka, T., Togashi, S., Kamioka, H., Amakawa, H., Kagami, H., Hamamoto, T., Yuhara, M., Orihashi, Y., Yoneda, S., Shimizu, H., 2000. JNdi-1: a neodymium isotopic reference in consistency with LaJolla neodymium. Chem. Geol. 168 (3–4), 279–281.

Tang, J., Xu, W., Niu, Y., Wang, F., Ge, W., Sorokin, A., Chekryzhov, I., 2016. Geochronology and geochemistry of Late Cretaceous–Paleocene granitoids in the Sikhote-Alin Orogenic Belt: Petrogenesis and implications for the oblique subduction of the paleo-Pacific plate. Lithos 266, 202–212.

Tang, J., Xu, W., Wang, F., Li, Y., Sun, C., Xiong, S., Wang, D., 2022. Temporal variations in the geochemistry of Mesozoic mafic–intermediate volcanic rocks in the northern Great Xing'an Range, Northeast China, and implications for deep lithospheric mantle processes. Lithos 422, 106721.

Ueda, H., Miyashita, S., 2005. Tectonic accretion of a subducted intraoceanic remnant arc in cretaceous Hokkaido, Japan, and implications for evolution of the Pacific northwest. Island Arc 14 (4), 582–598.

Van Horne, A., Sato, H., Ishiyama, T., 2017. Evolution of the Sea of Japan back-arc and some unsolved issues. Tectonophysics 710, 6–20.

Wang, F., Zhou, X.H., Zhang, L.C., Ying, J.F., Zhang, Y.T., Wu, F.Y., Zhu, R.X., 2006a. Late Mesozoic volcanism in the Great Xing'an Range (NE China): timing and implications for the dynamic setting of NE Asia. Earth Planet. Sci. Lett. 251 (1–2), 179–198.

Vervoort, J.D., Patchett, P.J., Blichert-Toft, J., Albarede, F., 1999. Relationships between Lu–Hf and Sm–Nd isotopic systems in the global sedimentary system. Earth Planet. Sci. Lett. 168 (1–2), 79–99.

Wang, P.J., Chen, F., Chen, S.M., Siebel, W., Satir, M., 2006b. Geochemical and Nd-Sr-Pb isotopic composition of Mesozoic volcanic rocks in the Songliao basin, NE China. Geochem. J. 40 (2), 149–159.

Wang, F., Xu, W.L., Xing, K.C., Tang, J., Wang, Z.W., Sun, C.Y., Wu, W., 2019. Temporal changes in the subduction of the Paleo-Pacific plate beneath Eurasia during the late

Mesozoic: Geochronological and geochemical evidence from Cretaceous volcanic rocks in eastern NE China. Lithos v. 326, 415–434.

Wang, T., Tong, Y., Xiao, W., Guo, L., Windley, B.F., Donskaya, T., Li, S., Tserendash, N., Zhang, J., 2022. Rollback, scissor-like closure of the Mongol-Okhotsk Ocean and formation of an orocline: magmatic migration based on a large archive of age data. Natl. Sci. Rev. 9 (5) p. nwab210.

Whalen, J.B., Currie, K.L., Chappell, B.W., 1987. A-type granites: geochemical characteristics, discrimination and petrogenesis. Contrib. Mineral. Petrol. 95 (4), 407–419.

White, A.J., Chappell, B.W., 1977. Ultrametamorphism and granitoid genesis. Tectonophysics 43 (1–2), 7–22.

Winchester, J.A., Floyd, P.A., 1977. Geochemical discrimination of different magma series and their differentiation products using immobile elements. Chem. Geol. 20, 325–343.

Wood, D.A., 1980. The application of a ThHfTa diagram to problems of tectonomagmatic classification and to establishing the nature of crustal contamination of basaltic lavas of the British Tertiary Volcanic Province. Earth Planet. Sci. Lett. 50 (1), 11–30.

Workman, R.K., Hart, S.R., 2005. Major and trace element composition of the depleted MORB mantle (DMM). Earth Planet. Sci. Lett. 231 (1–2), 53–72.

Wu, J.T.J., Wu, J., 2019. Izanagi-Pacific ridge subduction revealed by a 56 to 46 Ma magmatic gap along the northeast Asian margin. Geology 47 (10), 953–957.

Wu, F.Y., Jahn, B.M., Wilde, S.A., Lo, C.H., Yui, T.F., Lin, Q., Ge, W.C., Sun, D.Y., 2003. Highly fractionated I-type granites in NE China (I): geochronology and petrogenesis. Lithos 66 (3–4), 241–273.

Wu, J., Suppe, J., Lu, R., Kanda, R., 2016. Philippine Sea and East Asian plate tectonics since 52 Ma constrained by new subducted slab reconstruction methods. J. Geophys. Res. Solid Earth 121 (6), 4670–4741.

Wu, F., Liu, X., Ji, W., Wang, J., Yang, L., 2017a. Highly fractionated granites: recognition and research. Sci. China Earth Sci. 60 (7), 1201–1219.

Wu, J.T.J., Jahn, B.M., Nechaev, V., Chashchin, A., Popov, V., Yokoyama, K., Tsutsumi, Y., 2017b. Geochemical characteristics and petrogenesis of adakites in the Sikhote-Alin area, Russian Far East. J. Asian Earth Sci. 145, 512–529.

Wu, J., Lin, Y.A., Flament, N., Wu, J.T.J., Liu, Y., 2022a. Northwest Pacific-Izanagi plate tectonics since Cretaceous times from western Pacific mantle structure. Earth Planet. Sci. Lett. 583, 117445.

Wu, J.T.J., Wu, J., Okamoto, K., 2022b. Intra-oceanic arc accretion along Northeast Asia during Early Cretaceous provides a plate tectonic context for North China craton destruction. Earth Sci. Rev. 103952.

Xiao, W., Song, D., Windley, B.F., Li, J., Han, C., Wan, B., Zhang, J., Ao, S., Zhang, Z., 2020. Accretionary processes and metallogenesis of the Central Asian Orogenic Belt: advances and perspectives. Sci. China Earth Sci. 63 (3), 329–361.

Xu, J., Ben-Avraham, Z., Kelty, T., Yu, H.S., 2014. Origin of marginal basins of the NW Pacific and their plate tectonic reconstructions. Earth Sci. Rev. 130, 154–196.

Yamasaki, T., Shimoda, G., Tani, K., Maeda, J., Nanayama, F., 2021. Subduction of the Izanagi-Pacific Ridge–transform intersection at the northeastern end of the Eurasian plate. Geology 49 (8), 952–957.

Zhang, Y.T., Sun, F.Y., Wang, S., Xin, W., 2018. Geochronology and geochemistry of Late Jurassic to Early Cretaceous granitoids in the northern Great Xing'an Range, NE China: petrogenesis and implications for late Mesozoic tectonic evolution. Lithos 312, 171–185.

Zhao, P., Jahn, B.M., Xu, B., 2017. Elemental and Sr-Nd isotopic geochemistry of cretaceous to early Paleogene granites and volcanic rocks in the Sikhote-Alin Orogenic Belt (Russian Far East): implications for the regional tectonic evolution. J. Asian Earth Sci. 146, 383–401.

Zhu, R., Zhao, G., Xiao, W., Chen, L., Tang, Y., 2021. Origin, accretion, and reworking of continents. Rev. Geophys. 59 (3) e2019RG000689.